THE GALAXY-MASS CORRELATION FUNCTION MEASURED FROM WEAK LENSING IN THE SDSS

Erin S. Sheldon,[1,2] David E. Johnston,[1,2] Joshua A. Frieman,[1,2,3] Ryan Scranton,[4] Timothy A. McKay,[5] A. J. Connolly,[4] Tamás Budavári,[6,7] Idit Zehavi,[8] Neta A. Bahcall,[9] J. Brinkmann,[10] and Masataka Fukugita[11]

Last revision 29-Nov-2003

ABSTRACT

We present galaxy-galaxy lensing measurements over scales 0.025 to 10 h^{-1} Mpc in the Sloan Digital Sky Survey. Using a flux-limited sample of 127,001 lens galaxies with spectroscopic redshifts and mean luminosity $\langle L \rangle \sim L_*$ and 9,020,388 source galaxies with photometric redshifts, we invert the lensing signal to obtain the galaxy-mass correlation function ξ_{gm}. We find ξ_{gm} is consistent with a power-law, $\xi_{gm} = (r/r_0)^{-\gamma}$, with best-fit parameters $\gamma = 1.79 \pm 0.06$ and $r_0 = (5.4 \pm 0.7)(0.27/\Omega_m)^{1/\gamma}h^{-1}$ Mpc. At fixed separation, the ratio $\xi_{gg}/\xi_{gm} = b/r$ where b is the bias and r is the correlation coefficient. Comparing to the galaxy auto-correlation function for a similarly selected sample of SDSS galaxies, we find that b/r is approximately scale independent over scales $0.2 - 6.7h^{-1}$ Mpc, with mean $\langle b/r \rangle = (1.3 \pm 0.2)(\Omega_m/0.27)$. We also find no scale dependence in b/r for a volume limited sample of luminous galaxies ($-23.0 < M_r < -21.5$). The mean b/r for this sample is $\langle b/r \rangle_{Vlim} = (2.0 \pm 0.7)(\Omega_m/0.27)$. We split the lens galaxy sample into subsets based on luminosity, color, spectral type, and velocity dispersion, and see clear trends of the lensing signal with each of these parameters. The amplitude and logarithmic slope of ξ_{gm} increases with galaxy luminosity. For high luminosities ($L \sim 5L_*$), ξ_{gm} deviates significantly from a power law. These trends with luminosity also appear in the subsample of red galaxies, which are more strongly clustered than blue galaxies.

Subject headings: cosmology:observations — dark matter — gravitational lensing — large-scale structure of the universe

1. INTRODUCTION

The measurement of galaxy clustering has long been a primary tool in constraining structure formation models and cosmology. Yet the power of galaxy surveys to discriminate between models is partially compromised by the fact that they provide only an indirect measure of the underlying mass distribution, subject to considerable uncertainties in the *bias*, that is, in how luminous galaxies trace the mass. In this context, the galaxy-mass cross-correlation function ξ_{gm} can provide important additional information, since it is in some sense a 'step closer' to the clustering of mass. Moreover, comparing ξ_{gm} with the galaxy auto-correlation function ξ_{gg} yields a measure of the bias and therefore a constraint on theories of galaxy formation. In this paper we measure the correlation between galaxies and mass using weak gravitational lensing.

[1] Center for Cosmological Physics, The University of Chicago, 5640 South Ellis Avenue Chicago, IL 60637
[2] Department of Astronomy and Astrophysics, The University of Chicago, 5640 South Ellis Avenue, Chicago, IL 60637.
[3] Fermi National Accelerator Laboratory, P.O. Box 500, Batavia, IL 60510.
[4] Department of Physics and Astronomy, University of Pittsburgh, 3941 O'Hara Street, Pittsburgh, PA 15260.
[5] Department of Physics, University of Michigan, 500 East University, Ann Arbor, MI 48109-1120.
[6] Department of Physics of Complex Systems, Eötvös University, Budapest, Pf. 32, H-1518 Budapest, Hungary.
[7] Department of Physics and Astronomy, The Johns Hopkins University, 3400 North Charles Street, Baltimore, MD 21218-2686.
[8] Steward Observatory, University of Arizona, 933 North Cherry Avenue, Tucson, AZ 85721.
[9] Princeton University Observatory, Peyton Hall, Princeton, NJ 08544.
[10] Apache Point Observatory, P.O. Box 59, Sunspot, NM 88349.
[11] Institute for Cosmic Ray Research, University of Tokyo, 5-1-5 Kashiwa, Kashiwa City, Chiba 277-8582, Japan.

In the current paradigm of structure formation, the formation of galaxies is heuristically divided into two parts. On large scales, cosmological parameters and the properties of the dark matter determine the growth of density perturbations and the eventual formation of massive dark halos. On smaller scales, hydrodynamic and other processes shape how luminous galaxies form within dark matter halos and how they evolve as halos accrete and merge. A natural consequence of this picture is that the galaxy distribution is related to but differs in detail from the mass distribution. This difference arises in part because halos are more strongly clustered than the dark matter as a whole, and more massive halos are more strongly clustered than less massive ones (Kaiser 1984). In addition, the efficiency of forming luminous galaxies of different types and luminosities varies (primarily) with halo mass.

The galaxy bias parameter can be defined in a number of ways, but a traditional one is as the ratio of the galaxy and mass auto-correlation functions at fixed separation (Kaiser 1984),

$$b^2 = \frac{\xi_{gg}}{\xi_{mm}} \quad . \tag{1}$$

The amplitude of the galaxy-mass cross-correlation ξ_{gm} relative to ξ_{gg} and ξ_{mm} can be expressed in terms of the correlation coefficient (Pen 1998),

$$r = \frac{\xi_{gm}}{(\xi_{mm}\xi_{gg})^{1/2}} \, , \tag{2}$$

so that $\xi_{gm} = br\xi_{mm}$. In general, b and r can be time-dependent functions of the pair separation and depend on galaxy properties. Since we will be comparing the galaxy-galaxy and galaxy-mass correlation functions, we

will constrain the ratio

$$\frac{\xi_{gg}}{\xi_{gm}} = \frac{b}{r} \ .$$ (3)

Galaxy surveys have provided a wealth of information on the behavior of the galaxy bias b as a function of galaxy luminosity and type. For example, on scales $r < 20h^{-1}$ Mpc, the clustering amplitude ξ_{gg} increases with luminosity (Norberg et al. 2001; Zehavi et al. 2002; Norberg et al. 2002; Zehavi et al. 2004), while the amplitude and shape of ξ_{gg} vary systematically from early to late galaxy types (Davis & Geller 1976; Norberg et al. 2001; Zehavi et al. 2002). Moreover, the nearly power-law behavior of ξ_{gg} as well as the small departures therefrom (Zehavi et al. 2003), combined with the assumption that the dark matter distribution is described by cold dark matter models, indicate that the bias is scale-dependent on these scales.

On larger scales, $r > 20h^{-1}$ Mpc, there is evidence from higher-order galaxy correlations (Frieman & Gaztañaga 1999; Szapudi et al. 2002; Verde et al. 2002), from the cosmic shear weak lensing power spectrum (Hoekstra et al. 2002b; Jarvis et al. 2003), and from comparison of the 2dF galaxy power spectrum (Percival et al. 2001) with the WMAP cosmic microwave background (CMB) temperature angular power spectrum (Spergel et al. 2003) that the linear galaxy bias parameter b_{lin} is of order unity for optically selected L_* galaxies. (Here, b_{lin}^2 is the ratio of the galaxy correlation function to the mass correlation function computed in linear perturbation theory; it is related but not identical to the bias defined in Equation 1.) Measurement of the parameter $\beta = \Omega_m^{0.6}/b_{lin}$ from redshift space distortions in galaxy surveys, combined with independent evidence that $\Omega_m \simeq 0.3$, also indicates $b_{lin}(L_*) \simeq 1$ on large scales (Peacock et al. 2001).

In recent years, weak gravitational lensing has become a powerful tool for probing the distribution and clustering of mass in the Universe. We focus on galaxy-galaxy lensing, the distortion induced in the images of background (source) galaxies by foreground lens galaxies. Although the typical distortion induced by a galaxy lens is tiny ($\sim 10^{-3}$) compared to the intrinsic ellipticities of the source galaxies (~ 0.3), the signals from a large sample of lens galaxies can be stacked, providing a mean measurement with high signal to noise. The mean lensing signal can be used to infer the galaxy-mass cross-correlation function which, when compared with the galaxy auto-correlation function, constrains the amplitude and scale dependence of the bias.

The first detection of galaxy-galaxy lensing was made by Brainerd et al. (1996), and the field has progressed rapidly since then (dell'Antonio & Tyson 1996; Griffiths et al. 1996; Hudson et al. 1998; Fischer et al. 2000; Wilson et al. 2001; Smith et al. 2001; McKay et al. 2002; Hoekstra et al. 2003a). The first high S/N measurements were made in the Sloan Digital Sky Survey (SDSS) (Fischer et al. 2000). Recent studies have benefited from improved data analysis and reduction techniques and from surveys which are specifically designed for lensing (Hoekstra et al. 2001). Most work in galaxy lensing has concentrated on its power to constrain galaxy halo parameters (Brainerd et al. 1996; Hudson et al. 1998; Fischer et al. 2000; Hoekstra et al. 2003a). However, galaxy lensing has also

been used to measure the bias directly (Hoekstra et al. 2001, 2002a); their results indicate that b and r are scale-dependent over scales $\sim 0.1 - 5h^{-1}$ Mpc, but that the ratio b/r is nearly constant at $b/r \simeq 1.1$ over this range.

A significant step forward in galaxy-galaxy lensing came with the use of samples of lens galaxies with spectroscopic redshifts (Smith et al. 2001; McKay et al. 2002). Lensing measurements could then be made as a function of physical rather than angular separation, placing lensing correlation measurements on a par with the auto-correlation measurements from galaxy redshift surveys. Incorporation of photometric redshifts for the source galaxies (Hudson et al. 1998) also substantially reduces errors in the lens mass calibration due to the breadth of the source galaxy redshift distribution.

In this paper, we study galaxy-mass correlations in the SDSS using weak gravitational lensing. Using a sample of 127,001 galaxies with spectroscopic redshifts and 9,020,388 galaxies with photometric redshifts, we measure the lensing signal with high S/N over scales from $0.025 - 10h^{-1}$ Mpc. This is the first galaxy lensing study to incorporate both spectroscopic lens redshifts and photometric source redshifts, it is by far the largest galaxy lens-source sample compiled, and it extends to scales larger than previous galaxy-galaxy measurements. A similar spectroscopic sample has been used for galaxy auto-correlation measurements in the SDSS (Zehavi et al. 2003). We compare the galaxy-mass and galaxy-galaxy correlations to constrain b/r over scales from 200 kpc to 10 Mpc. We also use the spectroscopic and photometric data from the SDSS to divide the lens galaxy sample by luminosity, color, spectral type, and velocity dispersion. We see clear dependences of ξ_{gm} on each of these properties.

The layout of the paper is as follows: In §2 we introduce lensing and the measurement methods. In §3 we discuss the SDSS data, reductions, and sample selection. The basic measurement of the lensing signal $\Delta\Sigma$ is presented in §4, and important checks and corrections for systematic errors using random points are discussed in §4.1. In §5-7 we use the data to infer the galaxy-mass correlation function ξ_{gm} and compare it with independent measurements of ξ_{gg} to constrain the bias. In §8-9 we explore the dependence of galaxy-mass correlations on galaxy luminosity and type. We conclude in §10 and discuss possible systematic errors in the Appendix.

Throughout this paper, where necessary we use a Friedman-Robertson-Walker cosmology with $\Omega_M = 0.27$, $\Omega_\Lambda = 0.73$, and H$_0 = 100$ h km/s. All distances, densities, and luminosities are expressed in comoving coordinates.

2. LENSING AND GALAXY-MASS CORRELATIONS

2.1. *Gravitational Shear and the Galaxy-mass Correlation Function*

In this section we review the relation between the induced shear, which can be estimated from source galaxy shape measurements, the galaxy-mass cross correlation function ξ_{gm}, and the projected cross-correlation function w_{gm}. The tangential shear, γ_T, azimuthally averaged over a thin annulus at projected radius R from a lens galaxy, is directly related to the projected surface

mass density of the lens within the aperture,

$$\gamma_T \times \Sigma_{crit} = \overline{\Sigma}(< R) - \overline{\Sigma}(R) \equiv \Delta\Sigma \; , \qquad (4)$$

where $\overline{\Sigma}(< R)$ is the mean surface density within radius R, and $\overline{\Sigma}(R)$ is the azimuthally averaged surface density at radius R (Miralda-Escude 1991; Kaiser et al. 1994; Wilson et al. 2001). The proportionality constant Σ_{crit} encodes the geometry of the lens-source system,

$$\Sigma_{crit}^{-1} = \frac{4\pi G D_{LS} D_L}{c^2 D_S} \; , \qquad (5)$$

where D_L, D_S, and D_{LS} are angular diameter distances to lens, source, and between lens and source.

Due to the subtraction in equation 4, uniform mass sheets (such as the mean density of the universe $\overline{\rho} = \Omega_m \rho_{crit}$) do not contribute to $\Delta\Sigma$—it measures the mean *excess* projected mass density. The mean excess mass density at radius r from a galaxy is $\overline{\rho}\,\xi_{gm}(r)$. The mean excess projected density $\Sigma(R)$ is given by the radial integral:

$$\langle\Sigma(R)\rangle = \int \overline{\rho}\xi_{gm}(x,y,z)dz \equiv \overline{\rho}w_{gm}(R) \; , \qquad (6)$$

where w_{gm} is the projected galaxy-mass correlation function and $R = (x^2 + y^2)^{1/2}$ is the projected radius. The observable $\Delta\Sigma$ is itself an integral over $\Sigma(R)$ and hence w_{gm}:

$$\langle\Delta\Sigma(R)\rangle = \overline{\rho} \times \left[\frac{2}{R^2}\int_0^R R'dR' \; w_{gm}(R') - w_{gm}(R)\right] \qquad (7)$$

If the cross-correlation function can be approximated by a power-law in separation, $\xi_{gm} = (r/r_0)^{-\gamma}$, then w_{gm} can be written as

$$w_{gm}(R) = F(\gamma, r_0)R^{1-\gamma} \; , \qquad (8)$$

where $F(\gamma, r_0) = r_0^\gamma \Gamma(0.5)\Gamma[0.5(\gamma - 1)]/\Gamma(0.5\gamma)$ (Davis & Peebles 1983). In that case, the mean lensing signal $\Delta\Sigma$ is also a power law with index $\gamma - 1$ and is simply proportional to $\overline{\rho}w_{gm}$,

$$\langle\Delta\Sigma(R)\rangle = \left(\frac{\gamma - 1}{3 - \gamma}\right)\overline{\rho}w_{gm}(R) \; . \qquad (9)$$

More generally, the three-dimensional galaxy-mass correlation function can be obtained by inverting $\Delta\Sigma$ directly. Differentiating equation 7, we find

$$-\overline{\rho}\frac{dw_{gm}}{dR} = \frac{d\Delta\Sigma}{dR} + 2\frac{\Delta\Sigma}{R}. \qquad (10)$$

The derivative dw_{gm}/dR can be integrated to obtain ξ_{gm} using an Abell formula (Saunders et al. 1992):

$$\xi_{gm}(r) = \frac{1}{\pi}\int_r^\infty dR \frac{-dw_{gm}/dR}{(R^2 - r^2)^{1/2}} \qquad (11)$$

In practice, the data only cover a finite range of scales up to $r = R_{max}$. The estimated ξ_{gm} integrating to R_{max} is related to the true ξ_{gm} by

$$\xi_{gm}^{est}(r) = \xi_{gm}(r) - \frac{1}{\pi}\int_{R_{max}}^\infty dR \frac{-dw_{gm}/dR}{(R^2 - r^2)^{1/2}} \qquad (12)$$

where the last term reminds us of the (unknown) contribution from scales beyond those for which we have measurements. Provided the integrand falls sufficiently fast with separation, this term is negligible for scales r smaller than a fraction of R_{max}. Furthermore, since ξ_{gm} is linear in $\Delta\Sigma$, the covariance matrix of the latter can be straightforwardly propagated to that of the former.

2.2. Estimating $\Delta\Sigma$

We estimate the shear by measuring the tangential component of the source galaxy ellipticity relative to the the lens center, e_+, also known as the E-mode. In general, the shear is related in a complex way to e_+ (Schneider & Seitz 1995), but in the weak lensing regime the relationship is linear:

$$e_+ = 2\gamma_T \mathcal{R} + e_+^{int} \; , \qquad (13)$$

where e_+^{int} is the intrinsic ellipticity of the source, γ_T is the shear, and $\mathcal{R}$ is the "responsivity" (see equation 20). The assumption behind weak lensing measurements is that the source galaxies are randomly oriented in the absence of lensing, in which case their intrinsic shapes constitute a large but random source of error on the shear measurement. This "shape noise" is the dominant source of noise for most weak lensing measurements. We discuss limits on intrinsic correlations between galaxy ellipticities in the appendix.

The other component of the ellipticity, $e_\times$, also known as the B-mode, is measured at $45°$ with respect to the tangent. The average B-mode should be zero if the induced shear is due only to gravitational lensing (Kaiser 1995; Luppino & Kaiser 1997). This provides an important test for systematic errors, such as uncorrected PSF smearing, since they generally contribute to both the E- and B-modes.

In order to estimate $\Delta\Sigma$ from the shear, we must know the angular diameter distances D_L, D_S, D_{LS} for each lens-source pair (see equations 4 and 5). In the SDSS, we have spectroscopic redshifts for all the lens galaxies, so that D_L is measured to high precision (assuming a cosmological model). For the source galaxies, we have photometric redshift estimates (photoz), with typical relative errors of 20-30% (see §3.1.5), so there is comparable uncertainty in the value of Σ_{crit} for each lens-source pair.

Given the known redshifts of the lenses, the distribution of errors in the source galaxy ellipticity, and the distribution of errors in the photometric redshift for each source, we can write the likelihood for $\Delta\Sigma$ from all lens-source pairs,

$$\mathcal{L}(\Delta\Sigma) = \prod_{j=1}^{N_{Lens}} \prod_{i=1}^{N_{Source}} \int dz_s^i P(z_s^i) P(\gamma_T^i | z_s^i, z_L^j) \; , \quad (14)$$

where $\gamma_T^i = e_+^i/2\mathcal{R}$ is the shear estimator for the ith source galaxy, $P(z_s^i)$ is the probability distribution for its redshift (the product of the Gaussian error distribution returned by the photoz estimator and a prior based on the redshift distribution for the source population; see §3.1.5), and $P(\gamma_T^i | z_s^i, z_L^j)$ is the probability distribution of the shear given the source and lens redshifts, which is a function of the desired quantity $\Delta\Sigma$:

$$P(\gamma_T^i | z_s^i, z_L^j) \propto$$
$$\exp\left(-\frac{1}{2}\left[\frac{\gamma_T^i - \Delta\Sigma \times \Sigma_{crit}^{-1}(z_s^i, z_L^j)}{\sigma(\gamma_T^i)}\right]^2\right) \qquad (15)$$

In equation 15, $4 \times \sigma^2(\gamma_T^i) = \sigma^2(e_+^i) + \sigma_{SN}^2$: the shear uncertainty is the sum of the measurement variance $\sigma^2(e_+^i)$ and the intrinsic variance in the shapes of the source galaxies $\sigma_{SN}^2 = \langle(e_+^{int})^2\rangle$. The shape noise measured

from bright, well-resolved galaxies is $\sigma_{SN} \approx 0.32$, and the typical measurement error $\sigma(e_+)$ ranges from ~ 0.05 for $r=18$ to ~ 0.4 for $r=21.5$. The intrinsic shape distribution is not Gaussian as we have assumed in equation 15, but it is symmetric. Monte Carlo simulations indicate that this approximation does not bias the measurement of $\Delta\Sigma$ within our measurement uncertainties, provided we take σ_{SN} as the standard deviation of the non-Gaussian shape distribution.

Although the typical uncertainty in the source galaxy photometric redshifts is 20-30%, this is small compared to the relative shear noise, which is typically $\sigma_{SN}/\gamma_T \sim 300\%$. Assuming shape error is the dominant source of noise, we can approximate equation 14 as

$$\log\mathcal{L}(\Delta\Sigma) = \sum_{j,i} \left(-\frac{1}{2} \left[\frac{\gamma_T^i - \Delta\Sigma \times \langle\Sigma_{crit}^{-1}\rangle_{j,i}}{\sigma(\gamma_T^i)} \right]^2 \right) \quad (16)$$

where we now use the critical surface density averaged over the photoz distribution for each source galaxy,

$$\langle\Sigma_{crit}^{-1}\rangle_{j,i} = \int dz_s^i P(z_s^i) \Sigma_{crit}^{-1}(z_s^i, z_L^j) \quad (17)$$

Monte Carlo simulations indicate that the true likelihood approaches this Gaussian approximation after stacking only a few hundred lenses.

The maximum likelihood solution is the standard weighted average,

$$\Delta\Sigma = \frac{\sum_{j=1}^{N_{Lens}} \sum_{i=1}^{N_{Source}} \Delta\Sigma_{j,i} w_{j,i}}{\sum_{j=1}^{N_{Lens}} \sum_{i=1}^{N_{Source}} w_{j,i}} , \quad (18)$$

where

$$\Delta\Sigma_{j,i} = \gamma_T^i / \langle\Sigma_{crit}^{-1}\rangle_{j,i}$$
$$w_{j,i} = \sigma_{j,i}^{-2}$$
$$\sigma_{j,i} = \sigma(\gamma_T^i) / \langle\Sigma_{crit}^{-1}\rangle_{j,i}. \quad (19)$$

Although this simple inverse variance weighting is not optimal (Bernstein & Jarvis 2002), it does lead to unbiased results and only a slight increase in the variance of $\Delta\Sigma$.

As indicated by equation 13, the ellipticity induced by a shear depends on the object's shear responsivity $\mathcal{R}$. A measure of how an applied shear alters the shape of a source, $\mathcal{R}$ depends on the object's intrinsic ellipticity and is similar to the shear polarizability of Kaiser et al. (1995). Following Bernstein & Jarvis (2002), we calculate a mean responsivity as a weighted average over all tangential ellipticities.

$$\mathcal{R} = \frac{\sum_{j,i} w_{j,i} \left[1 - k_0 - k_1(e_+^i)^2 \right]}{\sum_i w_{j,i}} , \quad (20)$$

where the weights are the same as in equation 19. We have again assumed a Gaussian distribution of ellipticities so that k_0 and k_1 are simple,

$$k_0 = (1-f)\sigma_{SN}^2, \quad k_1 = f^2,$$
$$f = \frac{\sigma_{SN}^2}{\sigma_{SN}^2 + \sigma^2(e_+^i)} \quad (21)$$

The mean $\mathcal{R}$ for our sources is 0.86.

3. DATA

The Sloan Digital Sky Survey (SDSS; York et al. (2000)) is an ongoing project to map nearly 1/4 of the sky in the northern Galactic cap (centered at $12^h 20^m$, $+32.8°$). Using a dedicated 2.5 meter telescope located at Apache Point Observatory in New Mexico, the SDSS comprises a photometric survey in 5 bandpasses (u, g, r, i, z; Fukugita et al. (1996)) to $r \sim 22$ and a spectroscopic survey of galaxies, luminous red galaxies, quasars, stars, and other selected targets. In addition, the survey covers 3 long, thin stripes in the southern Galactic hemisphere; the central southern stripe, covering ~ 200 square degrees, will be imaged many times, allowing time-domain studies as well as a deeper co-added image.

We select our lens galaxies from the SDSS main galaxy spectroscopic sample. For our background sources we use only well-resolved galaxies drawn from the photometric survey with well-measured photometric redshifts. Each sample is described in detail below.

3.1. Imaging Data

Imaging data are acquired in time-delay-and-integrate (TDI) or drift scan mode. An object passes across the camera (Gunn et al. 1998) at the same rate the CCDs read out, which occurs continuously during the exposure. The object crosses each of the 5 SDSS filters in turn, resulting in nearly simultaneous images in each bandpass. In order for the object to pass directly down the CCD columns, the distortion across the field of view must be exceedingly small. This is advantageous for lensing, since distortions in the optics cause a bias in galaxy shapes (§3.1.3). The distortion in the optics of the SDSS 2.5m telescope is negligible (Stoughton et al. 2002) and can be ignored.

The imaging data are reduced through various software pipelines, including the photometric (PHOTO, Lupton et al. (2001)), astrometric (Pier et al. 2003), and calibration (Hogg et al. 2001; Smith et al. 2002) pipelines, leading to calibrated lists of detected objects. The calibrated object lists are subsequently fed through various target selection pipelines (Eisenstein et al. 2001; Strauss et al. 2002; Richards et al. 2002) which select objects for spectroscopic followup.

The shape measurements discussed in §3.1.1 are implemented in PHOTO (v5_3), so we work directly with the calibrated object lists. These lists contain, among many other things, position (RA,DEC), several measures of the flux, diagnostic flags for the processing, and moments of the light distribution for each object and for the local Point Spread Function (PSF) (Stoughton et al. 2002). We augment the parameters measured by PHOTO with the probability that each object is a galaxy (§3.1.4) and with photometric redshifts.

3.1.1. Shape Measurements

Weak lensing measurements rely on the assumption that source galaxy shapes are an unbiased, albeit rather noisy, measure of the shear induced by foreground lenses. Therefore high S/N shape measurements and accurate corrections for bias are crucial for weak lensing measurements. For both shape measurements and corrections we use techniques described in Bernstein & Jarvis (2002)

(hereafter BJ02).

We determine the apparent shapes of objects from their flux-weighted second moments.

$$Q_{m,n} = \sum_{m,n} I_{m,n} W_{m,n} x_m x_n, \qquad (22)$$

where $I_{m,n}$ is the intensity at pixel m, n and $W_{m,n}$ is an elliptical Gaussian weight function, iteratively adapted to the shape and size of the object. Initial guesses for the size and position of the object are taken from the Petrosian radius and PHOTO centroid. Objects are removed if the iteration does not converge or if the iterated centroid wanders too far from the PHOTO centroid. The shape is parametrized by the polarization, or ellipticity, components, defined in terms of the second moments,

$$e_1 = \frac{Q_{11} - Q_{22}}{Q_{11} + Q_{22}} \qquad (23)$$

$$e_2 = \frac{2Q_{12}}{Q_{11} + Q_{22}}. \qquad (24)$$

The polarization is related directly to the shear via equation 13.

The errors in the moments are calculated from the photon noise under the assumption that each measurement is sky noise limited, which is a good approximation for the faint sources. Because the same pixels are used for measuring both components of the ellipticity, there is a small covariance between the components of the ellipticity. This covariance is also calculated and properly transformed when rotating to the tangential frame for shear measurements.

Because the natural coordinates for the SDSS are survey coordinates (λ, η) (Stoughton et al. 2002), we rotate the ellipticities into that coordinate system for the lensing measurements. The full covariance matrix for (e_1, e_2) is used to transform the errors under rotations. We combine the shape measurements from the g, r, and i bandpasses using the covariance matrices. This increases the S/N, simplifies the analysis, and reduces bandpass-dependent systematic effects. The u and z bands are much less sensitive and would contribute little to the analysis.

3.1.2. PSF Reconstruction

An anisotropic PSF, caused by instrumental and atmospheric effects, smears and alters the shapes of galaxies in a way which can mimic lensing. In addition, the finite size of the PSF—the seeing—tends to circularize the image, reducing the measured ellipticity. In order to correct for these effects, one should, in principle, determine the exact shape and size of the PSF at the position of every source galaxy. Imaging in drift scan mode produces images that are long, thin stripes on the sky. Because the PSF varies over time (along the direction of the scan) as well as across the camera, it must be tracked as a function of position in the overall image (see §3.1.3).

The photometric pipeline uses Karhunen-Loève (KL) decomposition (Hotelling 1933; Karhunen 1947; Loève 1948) to model the PSF (Lupton et al. 2001). The PSF is modeled on a frame-by-frame basis, where frames are defined as 2048×1490 pixel chunks composing the long SDSS image. A set of bright, isolated stars are chosen from ± 2 frames around the central frame, with typically

$15 - 25$ stars per frame. These stellar images $P_{(i)}(u, v)$ are used to form a set of KL basis functions or *eigen-images* $B_r(u, v)$, in terms of which the images can be reconstructed by keeping the first n terms in the expansion,

$$P_{(i)}(u, v) = \sum_{r=0}^{n-1} a_{(i)}^r B_r(u, v) \qquad (25)$$

where $P_{(i)}$ denotes the ith star, and u, v are pixel positions relative to the object center.

The spatial dependence of the coefficients $a_{(i)}^r$ are determined via a polynomial fit,

$$a_{(i)}^r \approx \sum_{l=m=0}^{l+m \leq N} b_{lm}^r x_{(i)}^l y_{(i)}^m \qquad (26)$$

where x, y are the coordinates of the center of the ith star relative to the center of the frame, N is the highest order in x, y included in the expansion, and b_{lm}^r are determined from minimizing

$$\chi^2 = \sum_i \left(P_{(i)}(u, v) - \sum_{r=0}^{n-1} a_{(i)}^r B_r(u, v) \right) \qquad (27)$$

Only the stars on $\pm 1/2$ a frame surrounding the given frame are used to determine the spatial variation, while stars from ± 2 frames are used to determine the KL basis functions.

In PHOTO, the number of terms used from the KL basis is usually $n = 3$; the order of the spatial fit is $N = 2$ unless there are too few stars, in which case the fit may be order 1 or even 0 (rare). To determine the coefficients b_{lm}^r, a total of $n(N+1)(N+2)/2$ constraints are needed, which may seem like too many for the typical number of available stars. There are many pixels in each star, however, so the number of spatial terms $(N+1)(N+2)/2 = 6$ (for quadratic fits) should be compared with the number of available stars.

The PSF is reconstructed at the position of each object and its second moments are measured; these are used in the analytic PSF correction scheme described in §3.1.3.

3.1.3. Shape Corrections

To correct galaxy shapes for the effects of PSF dilution and anisotropy, we use the techniques of BJ02 with the modifications specified in Hirata & Seljak (2002). Rather than a true deconvolution, this is an approximate analytic technique. The PSF is modeled as a transformation of the preseeing shape; to remove the effects of the PSF, the inverse transform must be calculated. This transformation is performed in shear space (or polarization space):

$$R * [(-e_{PSF}) \oplus e] = (-e_{PSF}) \oplus e_0 \qquad (28)$$

where e is the preseeing polarization, e_0 is the measured polarization, e_{PSF} is the polarization of the PSF, and R is the resolution parameter, which is related to the polarizability of Kaiser et al. (1995). The operator $\oplus$ is the shear addition operator defined in BJ02. If the shear addition operator were a simple addition, then equation 28 would reduce to:

$$e = [e_0 - (1 - R)e_{PSF}]/R \qquad (29)$$

For unweighted moments ($W_{m,n} = 1$) or if the objects and PSF have Gaussian surface brightness profiles, the formulae in BJ02 are exact, and the resolution parameter in this case is just $R = 1 - (s_{PSF}/s_{obj})^2$, where s is the linear size of the object or PSF. The light profiles of galaxies and of the PSF differ significantly from Gaussian, however. Furthermore, as noted in §3.1.1, we use a Gaussian radial weight function to optimize the S/N of object shape measurements. As a consequence, the resolution parameter R must be derived in an approximate way that accounts for both the weight function and the non-Gaussianity of the light profiles. For this work we use a weighted fourth moment to correct for higher order effects as discussed in BJ02 and Fischer et al. (2000).

3.1.4. *Star-Galaxy Separation*

To separate stars and galaxies cleanly at all magnitudes, we use the Bayesian method discussed in Scranton et al. (2002). The method makes use of the concentration parameter, which can be calculated from parameters output by `PHOTO`. The concentration is the difference between the object's PSF magnitude and exponential disk magnitude. The PSF magnitude is derived by fitting the local PSF shape to the object's light profile. The only free parameter in this fit is the overall flux. An exponential disk is also fit to the object, but in that case the scale length is also a free parameter. Thus, large objects have more flux in the exponential than the PSF fit and correspondingly large concentration, while stars have concentration around zero.

At bright magnitudes, galaxies and stars separate cleanly in concentration space. At fainter magnitudes, photometric errors increase and the distributions overlap. This is demonstrated in figure 1, which shows the distribution of concentration for objects with $20 < r < 21$ and $21 < r < 22$ drawn from 100 frames of a single SDSS imaging run (3325), with mean seeing of $1.25''$(typical of SDSS image quality). In bad seeing conditions, a smaller percentage of galaxies are larger than the PSF, again making separation difficult.

If we know the distribution in concentration for galaxies and stars as a function of seeing and magnitude, we can assign each object a probability P_g that it is a galaxy,

given its concentration, magnitude, and the local seeing. For our source galaxy sample, we can then select objects which have high values of P_g. To map out the distribution in concentration, we use regions from the SDSS Southern Survey which have been imaged many times. Some of these regions have been imaged as many as 16 times, with an average of about 8. By averaging the flux for each object from the multiple exposures to obtain higher S/N, a clean separation between the star and galaxy concentration distributions is achieved to fainter magnitudes. We have maps of the concentration distribution for $16 < r < 22$ and $0.9 < $ seeing $ < 1.8$, allowing us to accurately calibrate P_g and therefore define a clean galaxy sample. In the few regions of very bad seeing, we extrapolate the concentration conservatively, erring on the side of including fewer galaxies in the sample. In section 3.1.6 we discuss the cuts used for our source sample.

3.1.5. *Photometric Redshifts*

A photometric redshift (photoz) is estimated for each object in the source catalog. The repaired template fitting method is used, described in detail in Csabai et al. (2000) and implemented in the SDSS EDR (Csabai et al. 2003) as well as the DR1 (Abazajian et al. 2003). This technique uses the 5-band photometry for each object as a crude spectrum. The algorithm compares this spectrum to templates for different galaxy types at different redshifts. The result is an estimate of the type and redshift of each galaxy.

There is a large covariance between the inferred type of the galaxy and its photometric redshift. The code outputs a full covariance matrix for type and redshift. Because we do not use the type information, we use the error marginalized over type. We further assume that the resulting error is Gaussian, which is only a good approximation for high S/N measurements. This introduces a bias in the estimate of $\langle \Sigma_{crit}^{-1} \rangle$, but Monte Carlo simulations indicate that this is a negligible effect.

From comparisons to galaxies with known redshifts, the *rms* in the SDSS photoz estimates is found to be ~ 0.035 for $r < 18$, increasing to ~ 0.1 for $r < 21$. About 30% of our source galaxy sample has r between 21 and 22. Although the photozs are less reliable in this magnitude range, these objects receive relatively little weight in the analysis, because they have large shape errors and large photoz errors (and hence small $\langle \Sigma_{crit}^{-1} \rangle$).

The photoz distribution for the sources used in this study is shown in figure 2. The histogram shows the photometric redshifts, and the smooth curve is the distribution calculated by summing the Gaussian distributions for each galaxy. We use this smooth curve as a prior on the photometric redshift when calculating the inverse critical density for each lens-source pair (see §2.2). The large peaks in the distribution are most likely not real, but rather the result of degeneracies in the photometric redshift estimation. This issue is addressed further in the appendix.

Although there is significant overlap between the distribution of photozs and the distribution of lens redshifts (figure 4), sources with photozs in front of or near the lens redshift are given appropriately small weight according to equation 17.
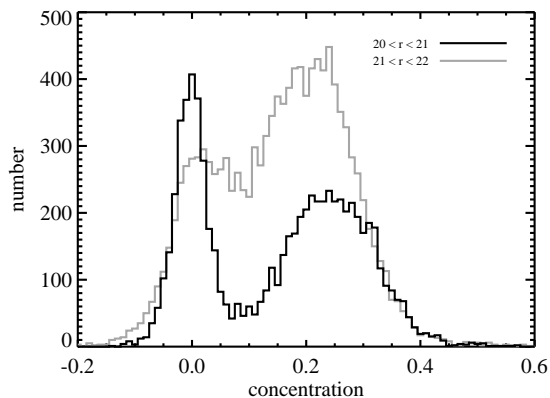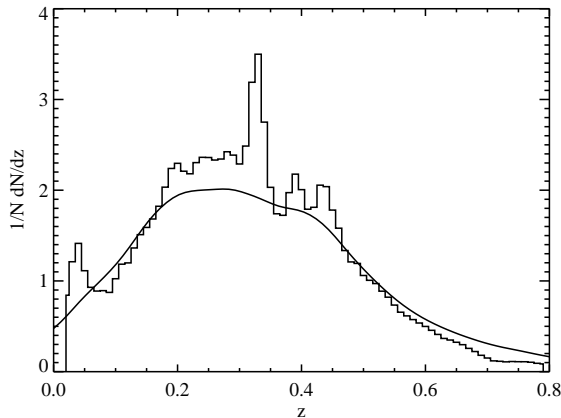

FIG. 1.— Concentration distribution for objects with $20 < r < 21$ (dark curve) and $21 < r < 22$ (light curve). Stars have concentration near zero. At faint magnitudes, stars and galaxies are not as easily separated.

FIG. 2.— Distribution of photometric redshifts for sources used in this study. The histogram shows the photozs in bins of $\Delta z = .01$, and the smooth curve is derived from summing the Gaussian distributions associated with each object.

3.1.6. *Defining the Source Sample*

Source galaxies are drawn from SDSS imaging stripes 9-15 and 27-37, covering a region of nearly 3800 square degrees. An Aitoff projection displaying the positions of these sources (as well as the lenses) is shown in figure 3. We make a series of cuts aimed at ensuring that the sample is of high purity (free from stellar contamination) and includes only well-resolved objects with usable shape information. We first require that the extinction-corrected r-band Petrosian magnitude is less than 22. We next make an object size cut, requiring that the resolution parameter $R > 0.2$. This removes most of the stars and unresolved galaxies from the sample. However, at faint magnitudes ($r > 21$), many stars and galaxies have similar values of R due to measurement error, so a further cut is needed. We employ the Bayesian galaxy probability (§3.1.4) and find that the combination $R > 0.2$, $P_g > 0.8$ guarantees that the source galaxy catalog is greater than 99% pure for $r < 21.5$ and greater than 98% pure for $21.5 < r < 22$.
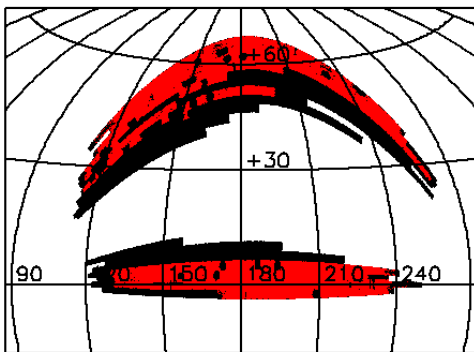

FIG. 3.— Aitoff projection showing the positions of the sources (black) and lenses (red) used in this study. The section covering the equator is stripes 9-15. The higher latitude section is stripes 27-37.

Additionally, we remove about ∼ 8% of the sources—

those with photoz errors greater than 0.4, and we further exclude objects with photoz less than 0.02 or greater than 0.8 since failed measurements tend to pile up at a photoz of 0.0 or 1.0. This removes another 10% of the objects. The final source catalog contains 9,020,388 galaxies, corresponding to a density of about $1 - 2$ source galaxies per square arcminute, depending on the local seeing.

3.2. *Spectroscopic Data*

The lens galaxies are selected from the SDSS "main" galaxy spectroscopic sample, which is magnitude- ($14.5 < r < 17.77$) and surface brightness-limited ($\mu_r < 23.5$), although these limits varied during the commissioning phase of the survey. See Strauss et al. (2002) for a description of "main" galaxy target selection.

SDSS spectroscopy is carried out using 640 optical fibers positioned in pre-drilled holes in a large metal plate in the focal plane. Targeted imaging regions are assigned spectroscopic plates by an adaptive tiling algorithm (Blanton et al. 2003), which also assigns each object a fiber. The spectroscopic data are reduced to 1-d spectra by SPECTRO2d, and the SPECTRO1d pipeline outputs redshift and an associated confidence level, spectral classification (galaxy, quasar, star), line measurements, and spectral type for galaxies, among other parameters (Stoughton et al. 2002). In addition, the velocity dispersion is measured for a large fraction of the early type galaxies.

For this analysis, we use a subset of the available spectroscopic "main" galaxy sample known as LSS sample12 (M. Blanton 2003, private communication). Although we draw from a larger sample, the mask (see §3.2.3) was produced for this subset. This sample is also being used for analysis of the galaxy auto-correlation function (Zehavi et al. 2004), while a slightly earlier sample (sample11) has been used to estimate the galaxy power spectrum (Tegmark et al. 2004). Using this sample allows us to make meaningful comparisons between the auto-correlation function and the galaxy-mass cross correlation function. The spectroscopic reductions used here are those of the SPECTRO1d pipeline, for which redshifts and spectroscopic classifications differ negligibly from those in the above references.

3.2.1. *Redshifts*

The SDSS spectra cover the wavelength range 3800-9200Å with a resolving power of 1800 (Stoughton et al. 2002). Repeated 15-minute exposures (totaling at least 45 minutes) are taken until the cumulative median $(S/N)^2$ per pixel in a fiber aperture is greater than 15 at $g = 20.2$ and $i = 19.9$ in all 4 spectrograph cameras. Redshifts are extracted with a success rate greater than 99%, and redshift confidence levels are greater than 98% for 95% of the galaxies. Repeat exposures of a number of spectroscopic plates indicates that "main" galaxy redshifts are reproducible to 30 km/s. We apply a cut on the redshift confidence level at > 75%, which removes 0.5% of the galaxies. Many galaxies are further removed during the lensing analysis, as discussed in §3.2.3 and §3.2.4. A redshift histogram is shown in figure 4 for the remaining 127,001 galaxies used in this work. The mean redshift for our sample using the relative weights from the lensing analysis is $\langle z \rangle = 0.1$.
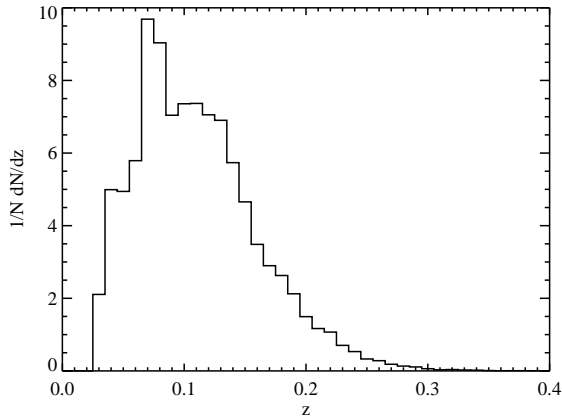
Fig. 4.— Redshift distribution for galaxies used in this study. This sample contains only "main" galaxy targets.

3.2.2. K-corrections

We apply K-corrections using the method discussed in Blanton et al. (2002) (kcorrect v1_10). Linear combinations of four spectral templates are fit to the five SDSS magnitudes for each galaxy given its redshift. Rest-frame absolute magnitudes and colors are then calculated. Figure 5 shows the distribution of absolute Petrosian magnitude for each of the 5 SDSS bandpasses.

3.2.3. Spectroscopic Masks

Because SDSS spectroscopy is taken through circular plates with a finite number of fibers of finite angular size, the spectroscopic completeness varies across the survey area. The resulting spectroscopic mask is represented by a combination of disks and spherical polygons (Tegmark et al. 2004). Our spherical polygon mask contains 3844 polygons covering an area of 2818 square degrees. Each polygon also contains the completeness, a number between 0 and 1 based on the fraction of targeted galaxies in that region which were observed. We apply this mask to the spectroscopy and include only galaxies from regions where the completeness is greater than 90%. The same criteria are used to generate the random points as discussed in 4.1.
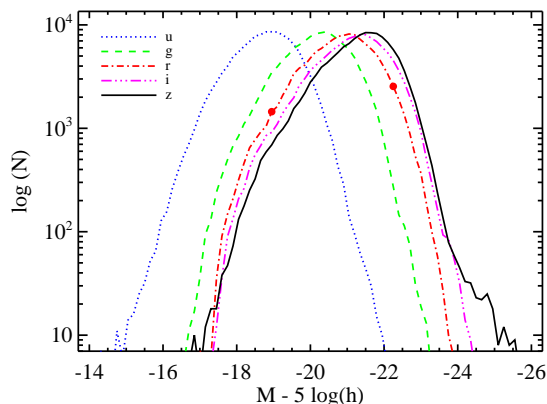

Fig. 5.— Distribution of rest-frame absolute magnitude in each of the 5 SDSS bandpasses for lenses used in this study. The filled circles mark the magnitude range for the flux limited sample of Zehavi et al. (2003). Ninety percent of our lens sample falls within this range.

3.2.4. Photometric Masks

Although the correction for PSF smearing (§3.1.3) substantially reduces the galaxy shape bias, it does not completely eliminate it—generally, a small, slowly varying residual remains. Fortunately, a residual PSF bias that is constant over the lens aperture cancels on average from the azimuthally averaged tangential shear, since two aligned sources separated by $90°$ relative to the lens contribute equally but with opposite sign. To take advantage of this cancellation, we divide the source galaxies around each lens into quadrants and demand that at least two adjacent quadrants are free of edges and holes out to the maximum search radius.

We represent the geometry of the sources using the hierarchical pixel scheme SDSSPix[1] (Scranton et al. 2003), modeled after a similar scheme developed for CMB analysis (Gòrski et al. 1998). This scheme represents well the rectangular geometry of the SDSS stripes. The mask is a collection of pixels at varying resolution covering regions with holes or edges. We do not mask out bright stars (which cover only a tiny fraction of the survey area) for the lensing analysis.

After checking the spherical polygon masks (§3.2.3), each lens galaxy is checked against the pixel mask to guarantee that it is within the allowed region. Each quadrant around the lens is then checked to determine if it contains a hole or an edge. Lenses are excluded from the sample if there are no adjacent quadrants that are completely unmasked. In addition to this cut, we demand that the angular distribution of source galaxies around the lens have ellipticity no greater than 20% in order to ensure the availability of pairs with $90°$ separation. The same criteria are applied to the random points (see §4.1).

We draw the final spectroscopic data set from SDSS stripes $9 - 12$ (near the equator) and $28 - 37$. We do not use galaxies from the 3 southern stripes (76,82,86), because they contain few lens-source pairs at large separation. Figure 3 shows the distribution of the lens and source galaxies as an Aitoff projection. After applying the cuts described above, the final lens sample contains 127,001 galaxies.

4. RESULTS: THE MEAN $\Delta\Sigma$ FROM $.02 - 10h^{-1}$ Mpc

The mean lensing signal $\Delta\Sigma$ for the full sample of SDSS lens galaxies is shown in figure 6. The signal is unambiguously detected from 25 h^{-1} kpc to 10 h^{-1}Mpc. The corresponding mean shear γ_T is shown on the right axis. Corrections have been made to this profile as described in §4.1. These corrections are relatively small in all radial bins.

The errors in figure 6 come from jackknife re-sampling. Although we expect statistical errors to dominate over sample variance even on the largest scales shown here, there are in addition large variations in the systematic errors. Due to gaps between the 5 CCD columns, two interleaving imaging runs make up a contiguous imaging stripe, and they are generally taken on different nights under different photometric conditions. As a result, the residuals from the PSF correction vary between the columns of interleaving runs, each of which is ~ 0.2
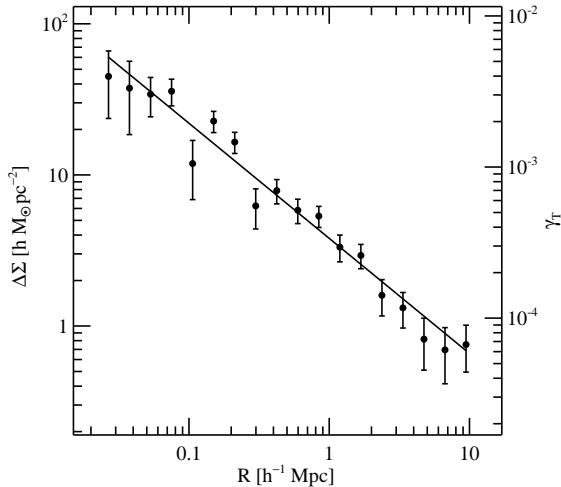
[1] http://lahmu.phyast.pitt.edu/~scranton/SDSSPix

FIG. 6.— Mean $\Delta\Sigma = \overline{\Sigma}(<R) - \overline{\Sigma}(R)$ measured for the full lens sample. The solid line is the best-fitting power law $\Delta\Sigma \propto R^{-0.76}$. The right axis shows the corresponding tangential shear γ_T.

degrees wide. The residuals also vary over time along the direction of the scan, with a typical scale of a few degrees. Thus the proper subsample size to account for this variation is about a square degree. We divide the sample into 2,000 disjoint subsamples, each approximately a square degree in size (see §3.2.3) and remeasure $\Delta\Sigma$ 2,000 times, leaving out each subsample in turn. Figure 7 shows an image of the resulting dimensionless correlation matrix $Corr_{i,j} = V_{i,j}/\sqrt{V_{i,i}V_{j,j}}$, where $V_{i,j} = \langle(\Delta\Sigma(R_i) - \langle\Delta\Sigma(R_i)\rangle)(\Delta\Sigma(R_j) - \langle\Delta\Sigma(R_j)\rangle)\rangle$. The off-diagonal terms are negligible in the inner bins but become important beyond $R \sim 1h^{-1}$ Mpc. The full covariance matrix is used for all model fitting.

The mean $\Delta\Sigma$ for the full sample is well described by a power law

$$\Delta\Sigma(R) = A(R/1\mathrm{Mpc})^{-\alpha} \qquad (30)$$

with $\alpha = 0.76 \pm 0.05$ and $A = (3.8 \pm 0.4)h\mathrm{M}_\odot\mathrm{pc}^{-2}$. The outliers at intermediate radii make the reduced χ^2 for the power law fit somewhat poor but not unacceptable:
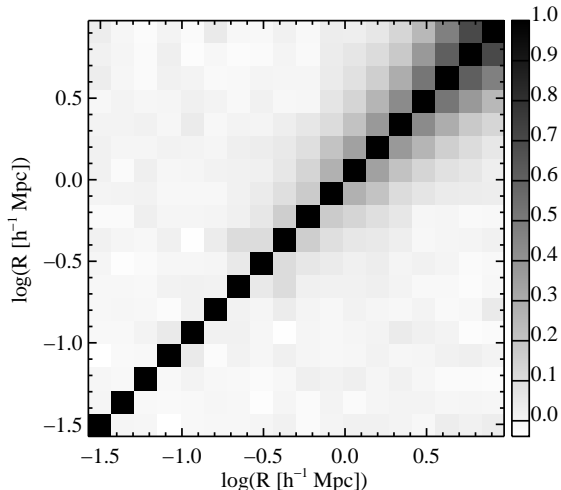

FIG. 7.— Correlation matrix for $\Delta\Sigma$ in figure 6 calculated using jackknife re-sampling.

$\chi^2/\nu = 1.26$. There is a 20% chance of χ^2 exceeding this value randomly.

An important check for systematic errors is the "B-mode", $\Delta\Sigma_\times$ the average shear signal measured at 45° with respect to the tangential component. If the tangential shear signal is due solely to lensing, the B-mode should be zero, whereas systematic errors generally contribute to both the E- and B-modes. The top panel of figure 8 shows $\Delta\Sigma_\times$ measured using the same source-lens sample used in figure 6. This measurement is consistent with zero.

4.1. Systematics Tests with Random Points

By replacing the lens galaxies with sets of random points, we can gauge two systematic effects on $\Delta\Sigma$: residuals in the PSF correction and the radial bias due to clustering of sources with the lenses. We generated a random sample with ten times as many points as the lens sample, using the same masks and selection criteria described in §3.2.3 and §3.2.4. The random points are drawn from the same redshift distribution as the lens galaxies. These criteria guarantee that the same regions, and thus roughly the same systematics, are sampled by the lenses and the random points. Any non-zero lensing signal for the random points we ascribe to residuals in the PSF correction.

The bottom panel of figure 8 shows $\Delta\Sigma$ measured around 1,270,010 random points, with errors from jackknife re-sampling. Note that the random sample is large enough that in this case sample variance dominates the error in the outer bins. There is a significant signal at large radius. The signal at smaller radii is less well determined, but it is in any case far below the signal due to lenses. Interpreting the large-scale signal as systematic error, we subtract it from the $\Delta\Sigma$ measured around lenses and add the errors $\sigma^2_{final} = \sigma^2_{lens} + \sigma^2_{rand}$; this correction is incorporated in figure 6.
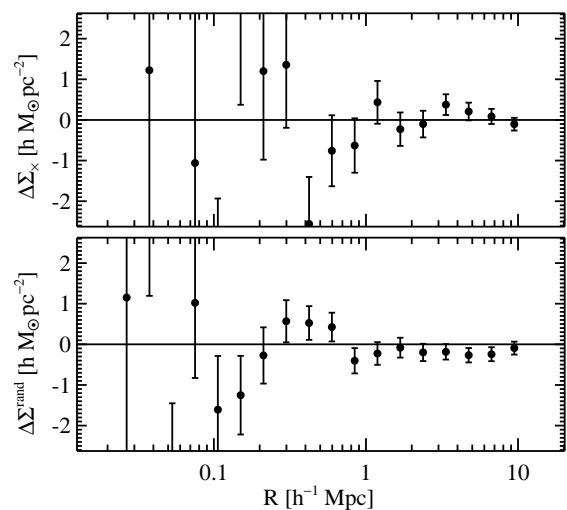

FIG. 8.— Two tests for systematics in the lensing measurement. The top panel shows the "B-mode" for lensing, $\Delta\Sigma_\times$, measured around the same lenses used in figure 6. The measurement is consistent with zero, as expected for lensing. The bottom panel shows $\Delta\Sigma$ measured around 1,270,010 random points. The detection at large radius is indicative of systematic errors, most likely from residuals in the PSF correction. This has been subtracted from the signal around lenses for figure 6.

The second systematic probed by the random sample involves clustering of the source galaxies with the lenses. The calculation of the mean inverse critical density in §2.2 properly corrects for the fact that a fraction of the source galaxies are in front of the lenses, but only under the assumption that the lens and source galaxies are homogeneously distributed. Since galaxies are clustered, a small fraction of the sources are in fact physically associated with the lenses, causing a scale-dependent bias of the lensing signal. We correct for this by estimating the excess of sources around lenses compared with the random points. The correction factor is the ratio of the sums of the weights for sources around lenses and around random points:

$$C(R) = \frac{N_{rand}}{N_{lens}} \frac{\sum_{i,j} w_{i,j}}{\sum_{k,l} w_{k,l}} \qquad (31)$$

where i, j indicates sources found around lenses, k, l indicates sources found around random points, and $w_{i,j}$ is the weight for the lens-source pair (see §2.2). The value of $C(R) - 1$ is shown for the full sample in figure 9. The use of photometric redshifts reduces the correction significantly, since sources associated with the lenses are given little weight. We find that $C(R) - 1$ falls roughly as $R^{-0.9}$. The correction for clustered sources is essentially negligible beyond 50 kpc. The signal in figure 6 has been multiplied by $C(R)$.

We measure this correction factor separately for each of the lens subsamples presented in later sections. Since galaxy clustering increases with luminosity, and higher luminosity lens galaxies are seen out to higher redshift where more of the faint sources are near the lenses, the correction factor $C(R)$ increases with the luminosity of the lenses. The correction for our highest luminosity samples is 2.0 at 25 kpc compared to 1.1 for the full sample. Similarly, the correction for early type lens galaxies is larger, while the correction for late types is smaller than for the full sample. Although the corrections for

some samples are large, the value of the correction is well measured in each case.

We have also calculated the average $\Delta\Sigma$ for the luminosity subsamples defined below (§8). Because $C(R)$ depends on luminosity, the average of the subsamples could in principle differ from the mean $\Delta\Sigma$ estimated from the full sample, as suggested by Guzik & Seljak (2002) regarding the results of McKay et al. (2002). However, we find no significant difference in the two methods for our weighting scheme, which results in smaller corrections than those in McKay et al. (2002).

Note our calculation of $C(R)$ may be a slight over- or under-estimate, since lensing itself may induce some correlation between unassociated background sources and the positions of the foreground lenses through magnification. Lensing magnification can bring galaxies into a magnitude limited sample that would otherwise have been too faint to be included, and this effect will be a function of scale. On the other hand, the geometric distortion induced by the lens moves the apparent position of background galaxies radially outward, decreasing the number density. The net change in number density depends on magnification μ and the slope of the galaxy number counts s: the ratio of counts with and with out lensing is $N/N_0 \propto \mu^{(2.5s-1)}$ (Broadhurst et al. 1995). The magnification is of the same order as the shear, which for our lens sample is $\lesssim 10^{-3}$, and the slope s is typically about 0.4, which results in negligible magnification bias.

5. THE GALAXY-MASS CORRELATION FUNCTION

5.1. Power-law Fits to $\Delta\Sigma$

As noted in §2.1, a power-law $\Delta\Sigma$ is consistent, within the errors, with the galaxy-mass correlation function ξ_{gm} also being a power-law, $\xi_{gm} = (r/r_0)^{-\gamma}$, with slope $\gamma = 1 + \alpha$. Fitting for γ and r_0, we find best fit marginalized values of $\gamma = 1.76 \pm 0.05$ and $r_0 = (5.7 \pm 0.7)(0.27/\Omega_m)^{1/\gamma} h^{-1}$ Mpc. Because $\Delta\Sigma$ is proportional to $\overline{\rho}$, we have assumed a fiducial value for the mean density $\overline{\rho} = \rho_{crit}\Omega_m$ determined by WMAP + ACBAR + CBI in combination with the power spectrum from 2dF-GRS and Lyman α data, which yields $\Omega_m = 0.27 \pm 0.02$ (Spergel et al. 2003). Marginalizing over this small uncertainty in Ω_m does not change our error estimates.

5.2. Inversion to ξ_{gm}

In addition to fitting a power law to $\Delta\Sigma$, we performed a direct inversion of $\Delta\Sigma$ to ξ_{gm} as outlined in §2.1. ξ_{gm} for the main sample is shown in Figure 10. Again, since our measurements scale linearly with Ω_m, we have assumed a fiducial value of $\Omega_m = 0.27$.

In principle, the inversion from $\Delta\Sigma$ to ξ_{gm} at a given radius r requires data for $\Delta\Sigma$ to $R = \infty$. In practice, the contribution from scales beyond our data is negligible in all radial bins but the last few. We estimate the contribution from large scales by extrapolating the best-fit power law. Because the last point would be based entirely on the extrapolation, we exclude it from figure 10. The contribution of the extrapolation is small for the remaining points except for the last bin at 6.7 Mpc, for which it is a 40% effect.

Because we do not have any a priori knowledge of ξ_{gm} at large scales, we must include this extrapolation in
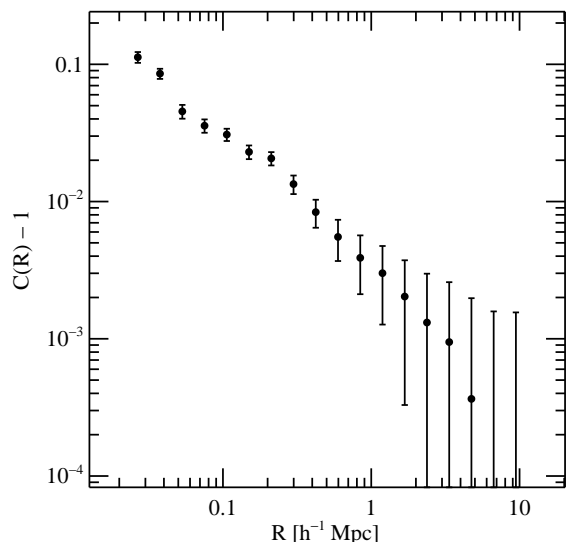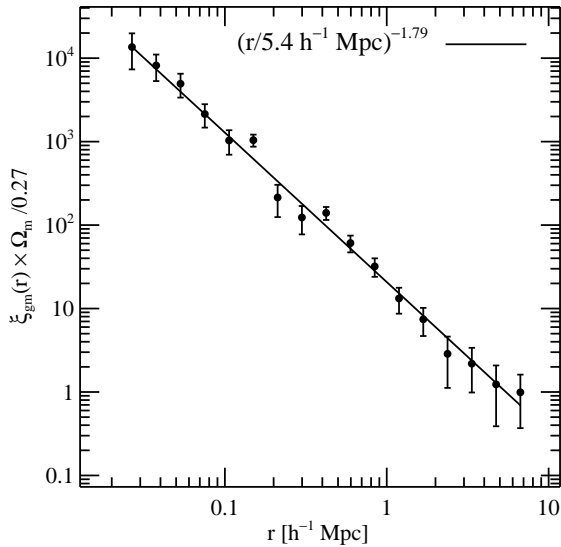

FIG. 9.— Correction factor for the clustering of sources around the lens galaxies. The function $C(R) - 1$ is essentially a weighted cross-correlation function between lenses and sources. The $\Delta\Sigma$ in figure 6 has been multiplied by $C(R)$, which is a negligible correction for radii larger than ~ 50 kpc.

FIG. 10.— Galaxy-mass cross-correlation function ξ_{gm}, obtained by inverting $\Delta\Sigma$. The amplitude of ξ_{gm} is degenerate with Ω_m, which we have set to 0.27. The solid line is the best-fit power law $\xi_{gm} = (r/5.4h^{-1} \text{ Mpc})^{-1.79}$.

the error budget. A lower bound on ξ_{gm} is obtained by assuming there is no signal beyond R_{max} at all: $\xi_{gm}^{low} = \xi_{gm}^{interior} - \sigma(\xi_{gm})$, where $\sigma(\xi_{gm})$ is the error on $\xi_{gm}^{interior}$ propagated from $\Delta\Sigma$. The most conservative error estimate is then $|\xi_{gm} - \xi_{gm}^{low}|$. This is the error plotted in figure 10 and is used for scaling the correlation matrix discussed below. Again, this only makes an significant difference in the last radial bin. This may still underestimate the upper bound on ξ_{gm} if in fact ξ_{gm} is considerably flatter at separations larger than R_{max}.

Due to the finite binning of $\Delta\Sigma$ (which is well described by a power law), linear interpolation results in a slight overestimate of the derivative $d\Delta\Sigma/dR$. A small ($\sim 4\%$) correction for this effect has been applied in figure 10.

Because the inversion is a linear operation on $\Delta\Sigma$, it is straightforward to obtain the covariance matrix for ξ_{gm}. The corresponding dimensionless correlation matrix is shown in figure 11. Due to the differentiation and integration involved in the inversion, adjacent points of ξ_{gm} are strongly correlated; i.e., the resulting covariance matrix for ξ_{gm} is less diagonal than the covariance matrix for $\Delta\Sigma$. The full covariance matrix is used for the model fits discussed below.

We fit ξ_{gm} to a power law model $\xi_{gm} = (r/r_0)^{-\gamma}$. For the inversion to ξ_{gm} we cannot use the last radial bin, so this fit only applies for $R < 6.7$ Mpc. The results are summarized in table 1. We find best-fit parameters $r_0 = (5.4\pm0.7)(0.27/\Omega_m)^{1/\gamma}$ and $\gamma = 1.79\pm0.06$, which are in agreement with the results we obtained fitting directly to $\Delta\Sigma$. These results are also in excellent agreement with the auto-correlation function from Zehavi et al. (2003). In the next section, we compare ξ_{gm} and ξ_{gg} directly to constrain the bias b/r.

6. BIAS

The ratio of the auto-correlation function ξ_{gg} to the galaxy-mass correlation function ξ_{gm} is a measure of the bias between galaxies and mass $\xi_{gg}/\xi_{gm} = b/r$ (see §1).

It is important to use the same galaxies for both ξ_{gm} and ξ_{gg}. We use the auto-correlation function from Zehavi et al. (2003) (hereafter Z03), measured for a flux limited sample of 118,000 SDSS "main" galaxies. The selection function for the Z03 sample is very similar to that of our lens sample, but the former covers a more restricted range of absolute magnitudes: $-22.2 < M_r < -18.9$, while our sample spans the range $-24 < M_r < -17$. However, figure 5 shows that 90% of the galaxies in our lens sample in fact lie within the Z03 magnitude range. Also, while each galaxy is weighted differently in the two correlation function measurements, the mean luminosities of the two samples are quite similar: for the Z03 sample, $\langle L_r \rangle = 1.7 \times 10^{10}h^{-2}L_\odot$, while the mean for our sample is $\langle L_r \rangle = 1.46 \times 10^{10}h^{-2}L_\odot$, both comparable to $L_* = 1.54 \times 10^{10}h^{-2}L_\odot$ (Blanton et al. 2001). Assuming that r_0 for ξ_{gg} scales with luminosity as in Norberg et al. (2001), we expect the auto-correlation length for our sample of galaxies to be only slightly lower than that of Z03, $r_0 = 5.60$ rather than $5.77h^{-1}$ Mpc.

Figure 12 shows ξ_{gm} (points with error bars) and the ξ_{gg} from Z03 (solid line). The ξ_{gg} was inferred by inverting from w_{gg}^p using the same techniques outlined in §2.1 (I. Zehavi, 2003, private communication). The amplitude of ξ_{gg} has been lowered by about 5% to account for the slight difference in mean luminosity for the two samples as discussed above. ξ_{gg} and ξ_{gm} for these samples are consistent within the errors over the common range of radii. The inverse galaxy-mass bias $r/b = \xi_{gm}/\xi_{gg}$ is shown in the bottom panel of figure 12. We use the inverse because ξ_{gm} is much noisier than ξ_{gg}. To calculate b/r, we have interpolated the points and errors from Z03. The bias b/r is consistent with unity and is scale independent within the errors. Fitting the bias to a constant over the radial range $0.2 - 6.7h^{-1}$ Mpc, we find

$$\langle b/r \rangle = (1.3 \pm 0.2)\left(\frac{\Omega_m}{0.27}\right). \quad (32)$$

7. GALAXY-MASS CORRELATIONS IN A VOLUME LIMITED SAMPLE OF LUMINOUS GALAXIES

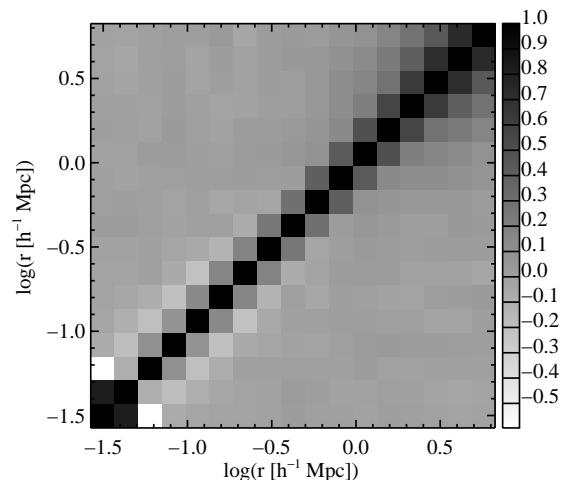In the previous section we used a flux limited sample to measure ξ_{gm}. This selection has the advantage that it

FIG. 11.— Correlation matrix for ξ_{gm} in figure 10, propagated from the covariance matrix of $\Delta\Sigma$.
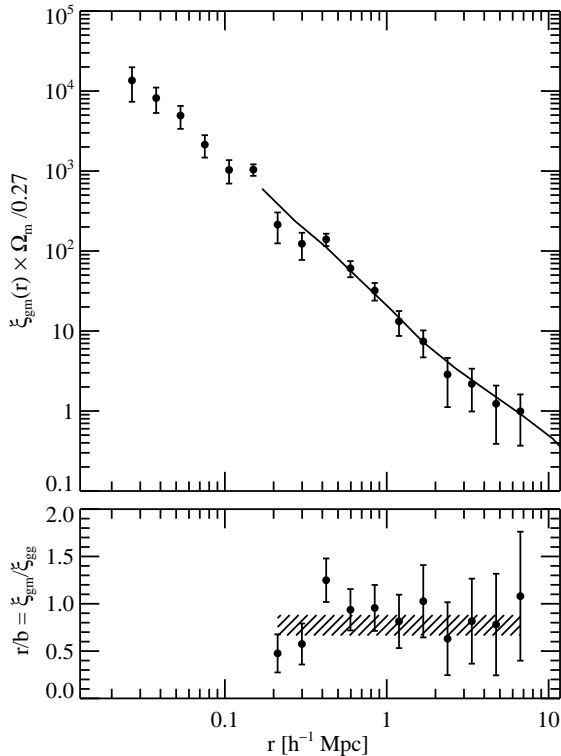
FIG. 12.— Galaxy-mass correlation function (filled circles) and the galaxy auto-correlation function (solid line) for similarly selected samples of SDSS galaxies. The top panel shows the two correlation functions and the bottom panel shows the inverse galaxy-mass bias $r/b = \xi_{gm}/\xi_{gg}$. We plot the inverse because ξ_{gm} is much noisier than ξ_{gg}. The bias is consistent with scale independent, with a mean of $\langle b/r \rangle = (1.3 \pm 0.2)(\Omega_m/0.27)$, shown as the hashed region.

uses the largest possible sample of lens galaxies and thus provides the best possible S/N measurement of ξ_{gm}. The interpretation is somewhat complicated, however, by the selection function. In order to provide a measurement that is simpler to interpret, we also defined a volume and magnitude limited sample, using the limits for the high-luminosity sample of Zehavi et al. (2002): $0.1 < z < 0.174$, $-23.0 < M_r - 5\log(h) < -21.5$, $\langle L_r \rangle = 3.96 \times 10^{10} L_\odot$. This sample contains 10,277 lenses.

The inferred ξ_{gm} for this sample is shown in the top panel of figure 13, along with ξ_{gg} inferred from the same volume and magnitude limited sample from Zehavi et al. (2002). Power law fits to ξ_{gm} are shown in table 1. The slope is significantly steeper than for the overall sample. ξ_{gm} shows deviations from a pure power-law, however, especially at small separations ($r < 0.2h^{-1}$ Mpc), and this is reflected in the poor reduced χ^2 for the power law fit. We will study the shape of ξ_{gm} as a function of luminosity in more detail in §8, where we split the overall sample into multiple bins in luminosity,

The bottom panel of figure 13 shows the inverse bias r/b over the common range of scales: $0.4 < r < 6.7h^{-1}$ Mpc. The b/r for this volume limited sample is consistent with scale-independent. The mean bias over these scales is

$$\langle b/r \rangle_{Vlim} = (2.0 \pm 0.7)\left(\frac{\Omega_m}{0.27}\right) \qquad (33)$$

Because this is a higher luminosity sample than the over-

all flux limited sample, one expects a larger bias (Norberg et al. 2001), but we do not yet detect any significant increase in the bias, as $\langle b/r \rangle_{Vlim}$ is consistent with $\langle b/r \rangle$ at the 1-σ level.

8. DEPENDENCE OF GALAXY-MASS CORRELATIONS ON LUMINOSITY

To study galaxy-mass clustering as a function of galaxy luminosity, we split the lens sample into three bins of luminosity separately in each of the five SDSS bandpasses, as shown in table 2. The binning is chosen primarily to yield comparable lensing S/N in each bin. To achieve this we place 85% of the galaxies in the lowest luminosity bin, 10% in the middle, and 5% in the highest bin. The low-luminosity bin must be so large because intrinsically faint galaxies are weakly clustered and are only detected in the SDSS at low redshift (for which the lensing efficiency is low). Since it contains the majority of lens galaxies, the faintest subsample has a mean luminosity comparable to the overall sample ($\sim L_*$), while the most luminous subsample is $\sim 5-6$ times brighter. Note that the number in each bin varies as a function of bandpass because galaxies are not detected in every bandpass. Also note that, while the different bins in luminosity are independent, the subsamples in the different bandpasses are simply re-samplings of the same lenses.

The mean $\Delta\Sigma$ for each luminosity subsample is shown in Figure 14. The profiles have been re-binned from 18 to 9 radial bins for clarity of presentation. Since the lowest luminosity subsample contains the large majority of lenses, the signal is comparable to that of the overall
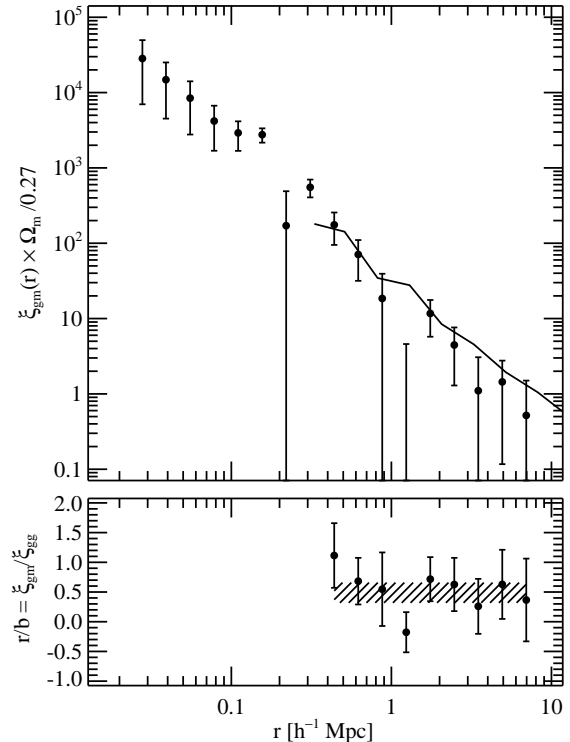

FIG. 13.— Same as figure 12, but for a volume and magnitude limited sample ($0.1 < z < 0.174$), ($-23.0 < M_r - 5\log(h) < -21.5$). The solid line is ξ_{gg} for the same selection criteria from Zehavi et al. (2002). We detect no scale dependence in the bias b/r. The mean bias over the common range of scales ($0.4 - 6.7h^{-1}$ Mpc) is $\langle b/r \rangle_{Vlim} = (2.0 \pm 0.7)(\Omega_m/0.27)$.

sample in both amplitude and shape. The higher luminosity subsamples show a significantly steeper slope on intermediate to large scales, and a flattening at smaller scales. This trend is seen in each of the bandpasses.

The $\Delta\Sigma$ for each luminosity bin was inverted to ξ_{gm} in the same way as for the overall sample. The resulting ξ_{gm} for each subsample is shown in figure 15. Note that the shape and relative amplitude of these data are independent of the assumed Ω_m.

ξ_{gm} for the highest luminosity bins deviate significantly from power laws, although this trend is less clear than for $\Delta\Sigma$. ξ_{gm} at large radius ($r > 1h^{-1}$ Mpc) is consistent across the different luminosity bins, while at intermediate radii ($0.1 < r < 1h^{-1}$ Mpc) the amplitude of the correlations increases with luminosity. On the smallest scales ($r < 0.1h^{-1}$ Mpc), the clustering increases weakly with luminosity. These trends are in qualitative agreement with the predictions from semi-analytic and n-body results from Guzik & Seljak (2001). Note, the low data points in ξ_{gm} for the middle (and highest) u-band luminosity bin is due to a single negative point in the unbinned $\Delta\Sigma$.

We fit the ξ_{gm} to power law models $\xi_{gm} = (r/r_0)^{-\gamma}$ for each of the luminosity subsamples. The results for these fits, summarized in table 2, indicate that ξ_{gm} for the low luminosity samples is a good fit to a power law and consistent with the overall sample. The two highest luminosity bins have a steeper logarithmic slope than the low luminosity sample. The highest luminosity bin, however, is a poor fit to a power law in each of the bandpasses. The fits over all radius give a slope of $\gamma \sim 2$. The slope for $r > 0.1$ Mpc is $\gamma \sim 2.5$, much steeper than the slope including the points at small radii. This is indicative of the rollover seen at small separations.

A priori, one might hypothesize that the change in slope from L_* to brighter galaxies is partly due to the fact that the higher luminosity subsamples are also redder: for the r-band samples, $g - r = 0.73(0.77)$ for the middle(brightest) sample, while $g - r = 0.63$ for the full sample (see table 2). However, the same increase of slope is also seen for the u subsamples, for which the trend of $g - r$ color with luminosity is much less pronounced.

9. DEPENDENCE OF GALAXY-MASS CORRELATIONS ON GALAXY SPECTRAL TYPE AND COLOR

In addition to luminosity, we can also study how the lensing signal varies with galaxy spectral type and color. The SPECTRO1d pipeline classifies galaxies as early to late spectral types using the method developed in Connolly et al. (1995) and Connolly & Szalay (1999). A Karhunen-Loève decomposition (KL) is performed on a large set ($\sim 100,000$) of galaxy spectra, ranging from quiescent E-Sc types to starburst irregulars. The spectrum of each galaxy is expanded in terms of the KL eigenspectra, and the first five coefficients of the expansion {ECOEFF1,..,ECOEFF5} are measured. Since most of the information is contained in the first two coefficients, a simple one-parameter family, constructed from the angle in the plane of the first two eigenvectors, provides a sufficient classification: ECLASS = $\tan^{-1}(-$ECOEFF2/ECOEFF1$)$. Early types have more negative ECLASS.

The distribution of ECLASS for the lens galaxy sample is shown in the bottom panel of figure 16. The rest frame $g - r$ distribution is also shown in the top panel. The $g - r$ color and ECLASS correlate well. We make cuts at ECLASS=-0.06 and $g - r = 0.7$ to split the sample into early/late types and red/blue. These cuts each divide the full sample roughly in half.

The mean $\Delta\Sigma$ for these different classes is shown in the top panel of figure 17. The red galaxies show a power law $\Delta\Sigma$ for $R > 100$ kpc and a flattening at smaller separations, similar to the two highest luminosity bins of the full sample. The blue and late type measurements, although noisy, are consistent with a power law $\Delta\Sigma$ over all separations.

The bottom panel of figure 17 shows the inversion of $\Delta\Sigma$ to ξ_{gm} for each class. The non-power law behavior for the early types is still visible for ξ_{gm} but it is less pronounced. The strong low feature in the blue/late samples is related to the feature at smaller radius in $\Delta\Sigma$; recall that the inversion to ξ_{gm} involves the derivative of $\Delta\Sigma$.

We fit a power law ξ_{gm} to each sample, using the full covariance matrix for the red/early samples, but only the diagonal elements for the blue/late samples because their covariance matrix is quite noisy. The results are shown in Table 1. The red/early type galaxies have a higher amplitude than the blue/late types, as indicated by the best-fit correlation length r_0. The red/early subsamples are also nearly twice as luminous as the blue/late subsamples. We detect no appreciable difference in the slope of the blue/late correlation function relative to that of the red/early types, in contrast to the strong shift in slope of the galaxy auto-correlation function as a function of type and color (Zehavi et al. 2002). On the other hand, the errors in the blue/late sample slopes are sizable, reflecting the lower S/N.

9.1. Dependence of ξ_{gm} on Luminosity for Red Galaxies

The lensing S/N for the red galaxy sample is quite high, allowing us to further subdivide this sample into three bins of luminosity in each of the 5 SDSS bandpasses, as we did in §8. The split is again 85%, 10%, and 5% of the galaxies in each of the three luminosity bins. The mean $\Delta\Sigma$ for these luminosity bins is shown in Figure 18, and the inversion to ξ_{gm} is shown in figure 19. The trends of $\Delta\Sigma$ and ξ_{gm} with red galaxy luminosity are similar to those for the full sample. The fits to power law correlation functions are listed in Table 3. Note that the correlation length r_0 and mean luminosity for each red luminosity subsample is larger than that of the corresponding full luminosity subsample, as expected from §9.

We now have two pieces of evidence suggesting that the increase in clustering strength and change in shape we observe is more closely associated with luminosity than with color: (i) for the subsamples split only by luminosity (not color), galaxies split by u-band luminosity show a significant increase of clustering strength with luminosity, and a change in shape, even though the mean $g - r$ color is nearly independent of luminosity for these subsamples; (ii) within the red galaxy sample itself, we find the same trends that we see for the full sample.

9.2. Dependence of ξ_{gm} on Velocity Dispersion

For a large fraction of the early type galaxies, selected by ECLASS and by the requirement that the surface brightness approximately fits a de Vaucouleurs pro-
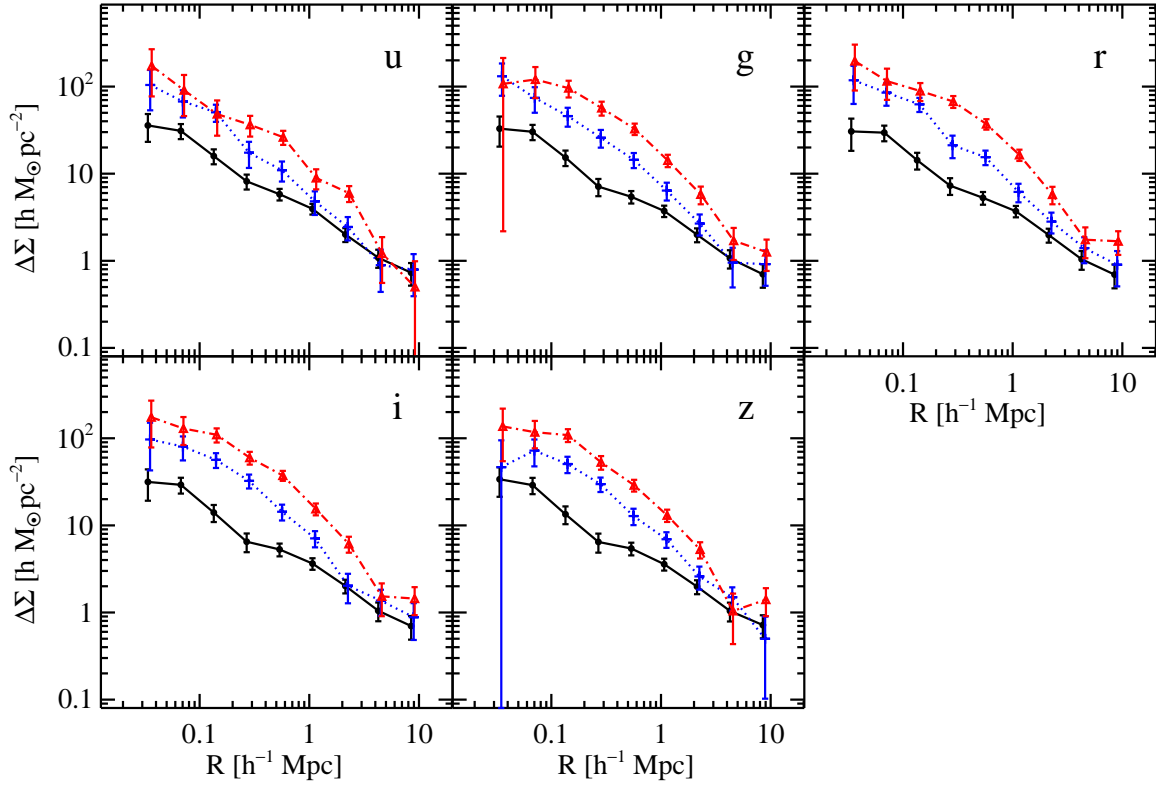
FIG. 14.— Mean $\Delta\Sigma$ in three luminosity subsamples for each of the 5 SDSS bandpasses. In each panel, circles connected by solid lines(black), crosses connected by dotted lines(blue), and triangles connected by dot-dashed lines(red) represent measurements for the lowest, middle, and highest luminosity subsamples. The data have been re-binned to 9 bins from 18 for clarity.
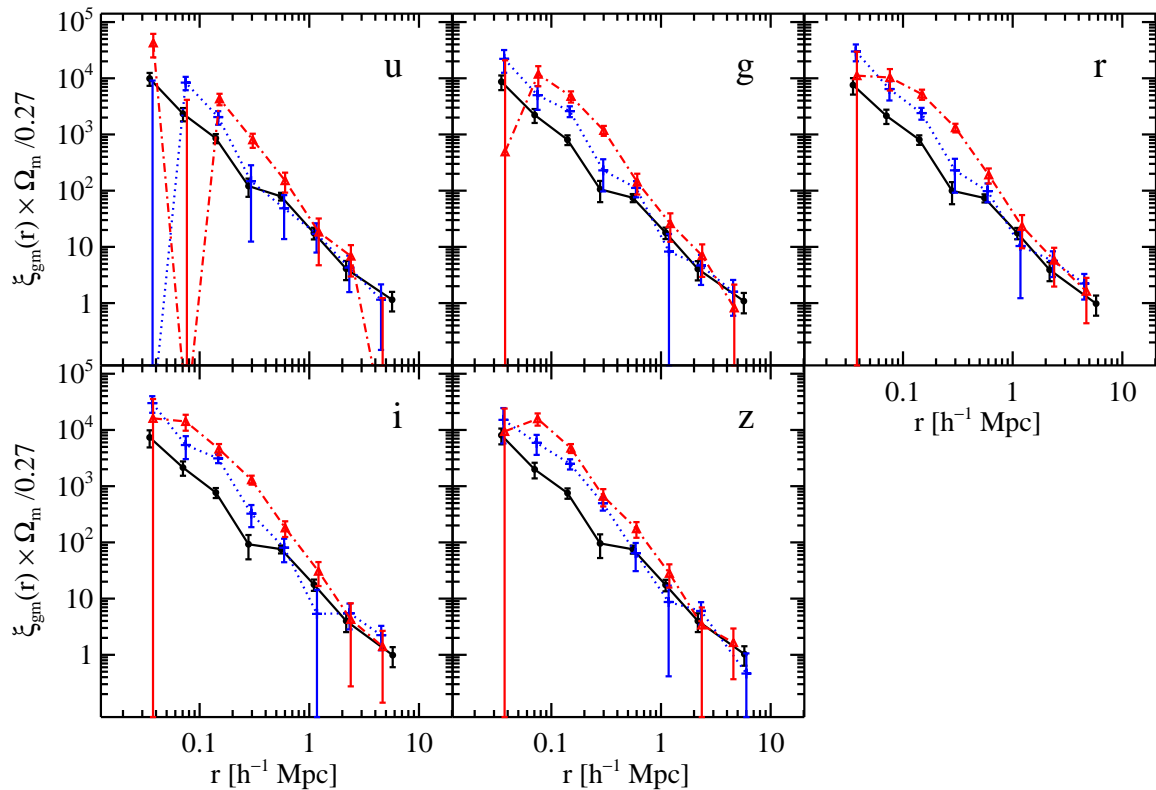

FIG. 15.— Same as figure 14, but now plotting ξ_{gm} obtained by inverting $\Delta\Sigma$. The highest luminosity bin shows significant deviation from a power law.
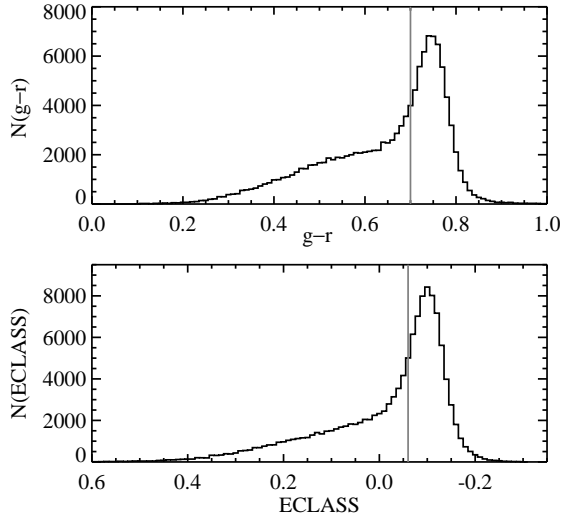
FIG. 16.— Distribution of $g-r$ (top panel) and ECLASS (bottom panel) for lens galaxies. Early types have more negative ECLASS, which has been plotted in reverse for comparison with $g-r$. We divide the samples at $g-r=0.7$ and ECLASS=-0.06 as shown by the gray vertical lines.

file, the SDSS spectroscopic pipeline measures the velocity dispersion σ_v. The distribution of velocity dispersions is shown in figure 20. We use only galaxies with $50 < \sigma_v(\mathrm{km/sec}) < 400$ for this study and split the sample roughly in half at $\sigma_v = 182$ km/sec. The low-σ_v sample has a mean of $\sigma_v = 143$ km/s and the high-σ_v sample has a mean of $\sigma_v = 215$ km/s.

In Figure 21 we show $\Delta\Sigma$ and ξ_{gm} for these two samples of early-type galaxies split by velocity dispersion. The half of the sample with higher σ_v shows a steeper slope, and a larger amplitude at $r < 500 h^{-1}$ kpc, than the low-σ_v galaxies. Interestingly, the amplitude for the low σ_v galaxies is actually somewhat higher that that for high-σ_v galaxies for $r > 1$Mpc. For neither sample is ξ_{gm} well fit by a power law. The shape of the high-σ_v ξ_{gm} is similar to that for the high luminosity red subsample. Given the Faber-Jackson relation between velocity dispersion and luminosity, this trend agrees qualitatively with the results above for the luminosity-scaling of ξ_{gm} for red galaxies.

10. DISCUSSION

We have presented measurements of the mean lensing signal $\Delta\Sigma = \overline{\Sigma}(< R) - \overline{\Sigma}(R)$ for a flux limited spectroscopic sample of SDSS galaxies with $\langle L \rangle \sim L_*$ and $\langle z \rangle \simeq 0.1$ over scales $25 h^{-1}$ kpc to $10 h^{-1}$ Mpc. $\Delta\Sigma$ is consistent with a power-law for all separations, with index 0.76 ± 0.05.

We performed a direct inversion to the three-dimensional galaxy-mass cross-correlation function ξ_{gm} over scales $0.025 - 6.7 h^{-1}$ Mpc[2]. The resulting ξ_{gm} is consistent with a power-law galaxy-mass correlation function over this range, $\xi_{gm} \times (\Omega_m/0.27) = (r/r_0)^{-\gamma}$. The measured slope, $\gamma = 1.79 \pm 0.06$ is consistent with the slope of the auto-correlation function ξ_{gg} for a similarly selected set of galaxies (Zehavi et al. 2003). We find that

[2] Modelers should predict $\Delta\Sigma$ if possible. It is higher S/N and contains more information than the inversion.
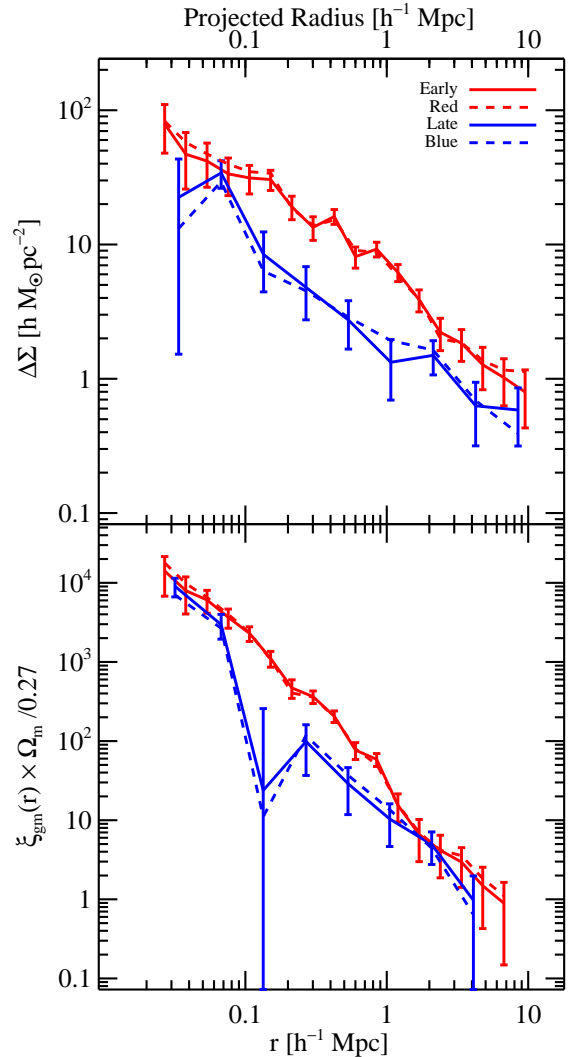

FIG. 17.— Mean $\Delta\Sigma$ and ξ_{gm} for different classes of galaxies. The top panel shows $\Delta\Sigma$ for galaxies classified as early or red in thick solid and dashed lines respectively(red). Late type and blue galaxies are shown in thin solid and dashed lines(blue). The trends for the ECLASS and $g-r$ cuts are very similar, as expected since color and spectral type are highly correlated. The bottom panel shows the inversion to ξ_{gm}.

the measured scale length, $r_0 = (5.4 \pm 0.7)(0.27/\Omega_m)^{1/\gamma}$, is also consistent with that of ξ_{gg} for the fiducial value of $\Omega_m = 0.27$, although the range of radii probed by the two data sets is quite different: the galaxy clustering results are measured for $r > 0.2 h^{-1}$ Mpc.

We compared ξ_{gm} with ξ_{gg} from Zehavi et al. (2003) over the common range of radii: $0.2 - 6.7 h^{-1}$ Mpc. The ratio of these functions is $\xi_{gg}/\xi_{gm} = b/r$, where b is the bias and r is the correlation coefficient at a fixed separation. We find that b/r is consistent with being scale independent over this range of scales, with a mean value of $\langle b/r \rangle = (1.3 \pm 0.2)(\Omega_m/0.27)$. Semi-analytic galaxy formation models suggest that b/r is a direct measure of the standard bias b, i.e., that r approaches unity for separations larger than 1 Mpc (Guzik & Seljak 2001), although there are hints from other lensing data that this may not be the case (Hoekstra et al. 2002a).

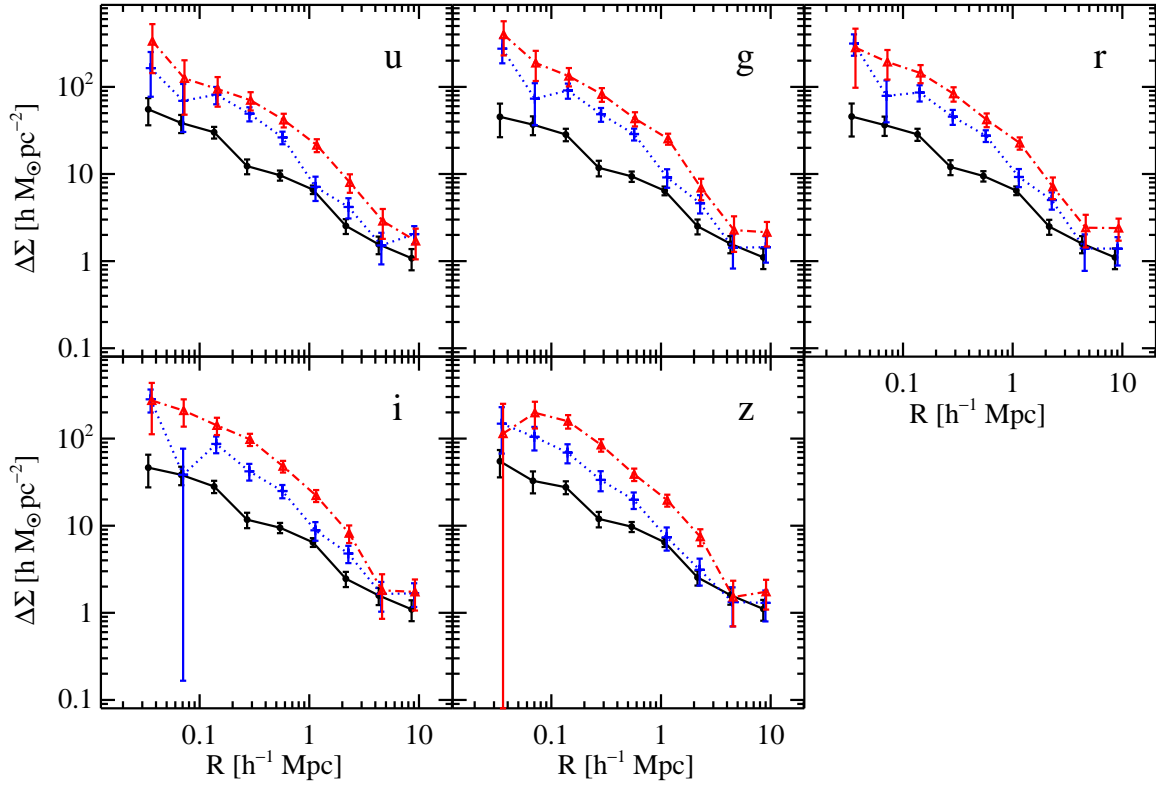We repeated this analysis for a volume and magnitude

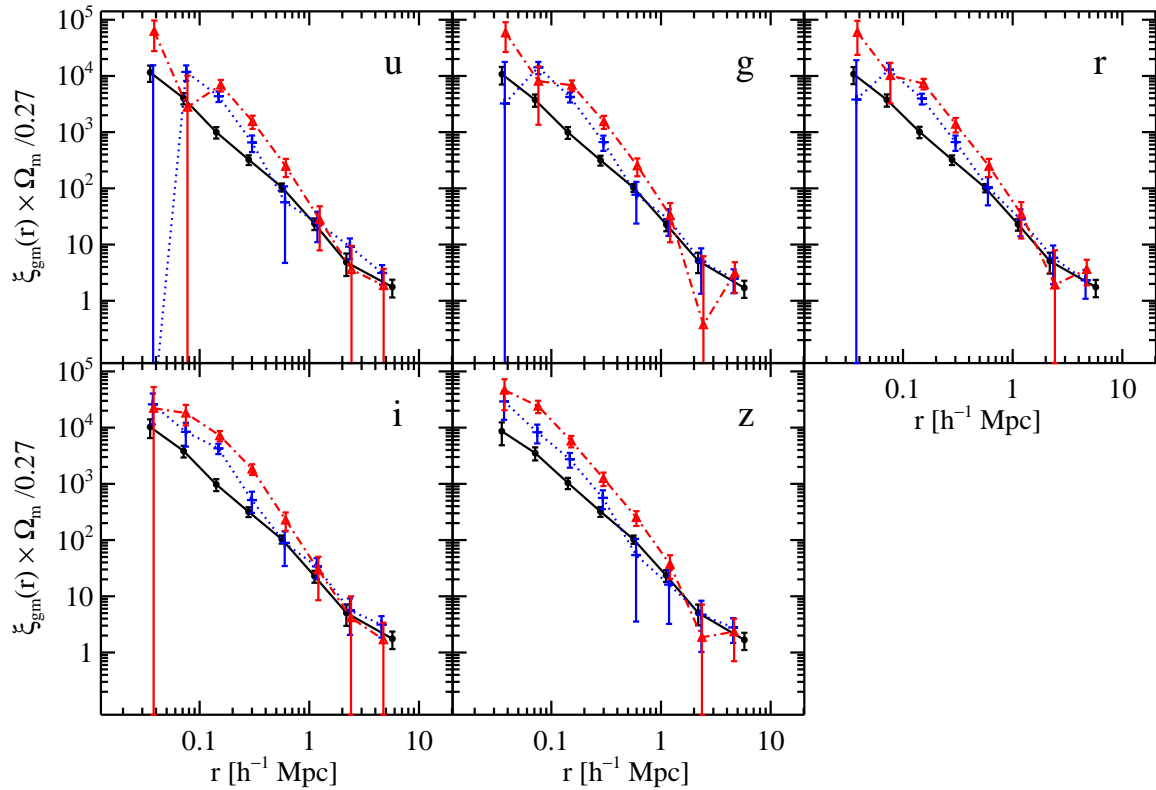Fig. 18.— Same as figure 14 but only for red galaxies, $g - r > 0.7$.

Fig. 19.— Same as figure 15 but only for red galaxies, $g - r > 0.7$.

limited sample of 10,277 luminous galaxies, with selection criteria designed to match that of the most luminous sample of Zehavi et al. (2002): $0.1 < z < 0.174$, $-23.0 < M_r - 5\log(h) < -21.5$. We detect no scale dependence in b/r, although ξ_{gm} for this sample is noisier than the overall sample. We find a mean b/r of $(2.0 \pm 0.7)(\Omega_m/0.27)$ over the common range of scales $(0.4 - 6.7h^{-1}$ Mpc$)$.

These results are consistent with and extend previous galaxy lensing measurements. Fischer et al. (2000) found a power law $\Delta\Sigma$ for angular scales $\theta < 600''$, or roughly $R < 1h^{-1}$ Mpc. Wilson et al. (2001) and Hoekstra et al. (2003a) (which incorporates some lens redshifts) found similar results over a smaller range of scales, although the power law index was less well constrained. The high precision measurements of Hoekstra et al. (2003b) show a power law on $\sim$2 Mpc scales (no power law fit is quoted). McKay et al. (2002), which used a smaller sample of SDSS lens galaxies with known redshifts, found a power law $\Delta\Sigma$ with slope consistent with the current study for $0.025 < R < 1h^{-1}$ Mpc. An model-dependent SDSS lensing analysis concentrating on small scales (Seljak et al. 2004, in preparation) found results consistent with those presented here. Hoekstra et al. (2002a) used a deeper, narrower sample than ours, without lens redshifts, to obtain a high S/N measurement of the shear over effective scales $R < 5h^{-1}$ Mpc. They find that b/r is approximately scale-dependent over the range $0.1 - 3h^{-1}$ Mpc, with mean amplitude $b/r = 1.09 \pm 0.04$ over these scales. However, combining their galaxy lensing data with deeper cosmic shear data, they measured both b and r. The errors in b and r are correlated, since both depend on the cosmic shear, but they found that b and r each vary with scale and track one another in such a way that the ratio b/r is approximately constant.

The value of b/r inferred above requires only the following assumptions: that general relativity is valid, the cosmological principle holds, and the FRW metric properly relates redshift to distance in our universe. We have explicitly shown the dependence on the parameter Ω_m (the dependence on other parameters through the angular diameter distance is weak for these redshifts). Further interpretation of these measurements requires further assumptions and model dependence. For example, if one believes that L_* galaxies are nearly unbiased tracers of
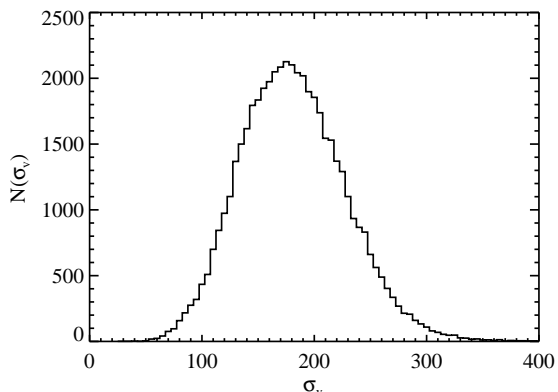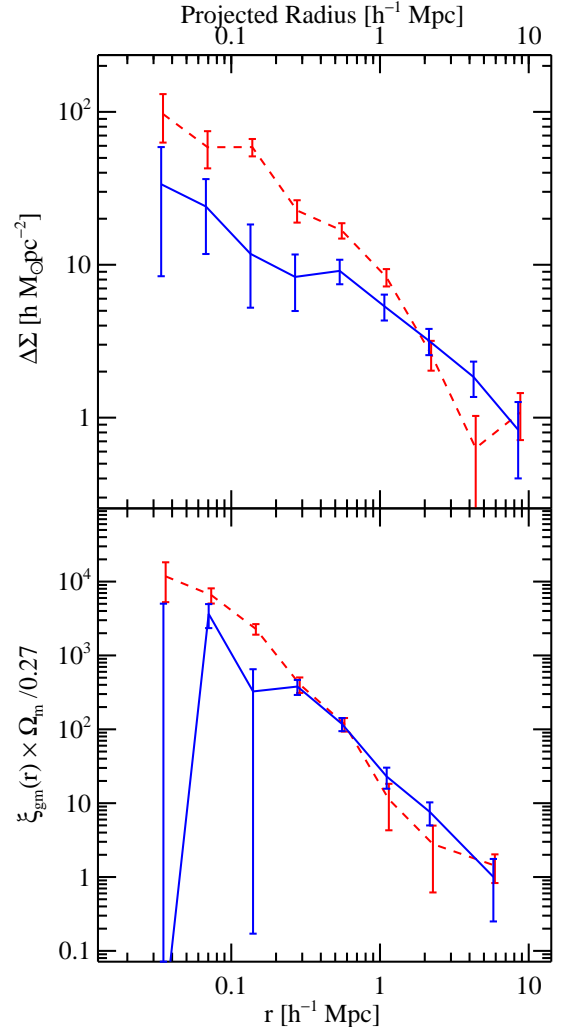

FIG. 21.— Mean $\Delta\Sigma$ and ξ_{gm} for early type galaxies with measured velocity dispersion $\sigma_v > 182$ km/sec (red-dashed curve) and < 182 km/sec (blue-solid curve). The amplitude for high σ_v galaxies is stronger at small scales, as expected from the trend with luminosity.

the mass on these scales, say $b/r = b_{lin} < 2$, then one can place a limit $\Omega_m < 0.6$ at 95% confidence. We leave it to the reader to further interpret these measurements in the context of particular models.

Splitting our lens galaxies into subsamples has enabled us to study ξ_{gm} as a function of luminosity, color, and spectral type. The amplitude of ξ_{gm} increases with increasing luminosity on intermediate $(0.1 - 1h^{-1}$ Mpc$)$ scales, consistent with the lower S/N results of McKay et al. (2002). However, we find that ξ_{gm} is nearly independent of luminosity on scales larger than $1h^{-1}$ Mpc (see figure 15). This is indicative of the increase in slope with luminosity on intermediate scales. The highest luminosity bin shows significant deviation from a power law, with a flattening at radii less than $0.1h^{-1}$ Mpc. These trends of the slope and amplitude of ξ_{gm} with luminosity are in good qualitative agreement with the predictions of semi-analytic galaxy formation models (Guzik & Seljak 2001). The semi-analytic models predict that the amplitude of ξ_{gm} increases with luminosity on small scales, but is only weakly dependent on luminosity for

FIG. 20.— Histogram of measured velocity dispersion σ_v for 49,024 early-type lens galaxies.

scales $r > 1h^{-1}$ Mpc, in agreement with our results.

The increase in clustering amplitude with luminosity on intermediate scales for ξ_{gm} is similar to that seen for the galaxy-autocorrelation function (Norberg et al. 2001; Zehavi et al. 2002), but the deviation from a power law on small scales at higher luminosity has not been seen in previous autocorrelation measurements. Also, the autocorrelation function shows a nearly equal increase in amplitude with luminosity on both large and intermediate scales (Norberg et al. 2001; Zehavi et al. 2002), but ξ_{gm} does not. This may imply a scale-dependent bias for high luminosities.

We have also detected a trend in ξ_{gm} with galaxy color and spectral type (figure 17). Red/early type galaxies show stronger correlation amplitude than blue/late types but the slopes of ξ_{gm} for the two subsamples are consistent within the errors. These results are consistent with the previous results of McKay et al. (2002). This behavior is also in qualitative agreement with the semi-analytic galaxy formation predictions (Guzik & Seljak 2001).

Finally, we have sufficient S/N to study the scaling of ξ_{gm} with luminosity and velocity dispersion for red/early type galaxies. Again, we find a similar increase in logarithmic slope and amplitude with luminosity on intermediate scales, and a weak luminosity dependence on large scales. We find the slope of ξ_{gm} increases with σ_v, but the high σ_v sample shows significant deviations from a power law.

A separate analysis will compare these results in detail with predictions from N-body simulations and the halo model of structure formation. A future study, using a larger lens sample, will concentrate on galaxy-galaxy lensing at small separations, where the signal is primarily sensitive to galaxy dark matter halos.

11. APPENDIX: PHOTOZ SYSTEMATIC ERRORS AND INTRINSIC ALIGNMENTS

We discussed two sources of systematic errors in §4.1: residuals from the PSF correction and clustering of faint sources around the lens galaxies. These biases have been estimated from the data and corrected for in our final results.

Another possible source of error may come from biases in the photometric redshifts (§3.1.5). Although the photometric redshift distributions inferred for SDSS galaxies are consistent with published redshift surveys for $r < 21$ (Csabai et al. 2003), there are well-known degeneracies in the technique (between type and redshift) that tend to push galaxies to particular values of photoz. This pile-up can be seen in figure 2: there are significant peaks in the photoz distribution at several redshifts. Although such peaks are often seen in spectroscopic redshift surveys, where they are associated with large-scale structures, the volume probed by the SDSS photoz sample is so large, containing ~ 4 million galaxies covering ~ 1000 square degrees out to $z \sim 0.6$, that the effects of such structures should be very small.

Because galaxies in parameter regions with strong degeneracies have relatively large photoz errors, we expect this bias to be suppressed in the final analysis. We have repeated our analysis using only the source galaxy redshift prior inferred from summing the individual Gaussians (as shown in figure 2), i.e., not using the photoz measurements for individual source galaxies, and we recover the same results within the noise. We have also used the method outlined in McKay et al. (2002), which uses the r magnitudes to infer the redshift distribution, and recover consistent results. Thus the bias from photoz degeneracies appears to be small compared to our statistical uncertainty.

Another issue that can possibly complicate interpretation of our results is intrinsic correlations in the ellipticities of the source galaxies. If the orientations of physically associated pairs of galaxies are correlated, this could possibly mimic a lensing signal.

Tidal torques can cause the angular momentum vectors of physically associated galaxies to be aligned (Crittenden et al. 2001). The magnitude of these ellipticity correlations is expected to be strong and relatively constant on scales less than ~ 1 Mpc, and decrease as ξ_{LS}, the correlation function of sources with lenses, on large scales (Crittenden et al. 2001). This effect has been seen in N-body simulations (Croft & Metzler 2000; Heavens et al. 2000) and there are possible detections in the Tully catalog (Pen et al. 2000) and SuperCOSMOS Sky Survey data (Brown et al. 2002), although these data are not ideal for such a study. The recent work of Heymans et al. (2003) suggests this effect may be near the low end of theoretical predictions.

It is not clear how intrinsic alignments affect tangential shear measurements. The tangential shear is the correlation between the position of a lens and the projection of source ellipticities onto the tangential reference frame, defined by a circle centered at the lens. The intrisic ellipticity correlations described above are correlations between pairs of ellipticities. There is little theoretical guidance about what tangential alignment to expect. For limits on this effect we turn to the recent study by Bernstein & Norberg (2002) which uses data from the 2dF redshift survey to study the tangential alignment of faint (2.2 magnitudes fainter than the primary) physically associated galaxies. They place an upper limit of $\langle e_+^{int} \rangle < 0.02(95\%)$ within $500\ h^{-1}$ kpc at $\langle z \rangle = 0.1$. A recent analysis of this tangential alignment within the

SDSS spectroscopic sample (Koester et al. 2003) places still more stringent limits on this tangential alignment $\langle e_+^{int} \rangle < 0.007(95\%)$ on $500h^{-1}$ kpc scales.

Most of the sources used in our study are far behind the lenses, in which case no correlation is expected between lens position and the tangential source galaxy ellipticity. A small fraction of sources, however, are actually faint companions of the foreground lenses. The fraction of physically associated sources is generally small (Fischer et al. 2000), and the use of photometric redshifts in our study down-weights these sources in the final analysis. The relative contribution of these objects in the lensing measurement is shown in figure 9. The mean contribution over 500 kpc is 0.018.

Assuming the result from Bernstein & Norberg (2002) also applies to our faint sources, we place a limit on the contamination from intrinsic alignments at $\langle e_+^{int} \rangle < 0.02 * 0.018 = 3.6 \times 10^{-4}$ on $500h^{-1}$ kpc scales. The mean distortion within this radius is $1.5 \pm 0.1 \times 10^{-3}$. Thus, on 500 h^{-1} kpc scales, the intrinsic alignments should contribute less than 20% of the signal at 95% confidence. The new SDSS results suggest the effect is smaller still ($< 8.5\%$). The intrinsic alignment correlations decrease with scale roughly as ξ_{LS}, and the relative contribution from the sources also decreases quickly with scale (figure 9). Thus, the contribution from intrinsic alignments should be small for radii $r \gtrsim 500h^{-1}$ kpc.

REFERENCES

Abazajian, K. et al. 2003, AJ, 126, 2081
Bernstein, G. M. & Jarvis, M. 2002, AJ, 123, 583
Bernstein, G. M. & Norberg, P. 2002, AJ, 124, 733
Blanton, M. R. et al. 2001, AJ, 121, 2358
—. 2002, in press (astro-ph/0205243)
—. 2003, AJ, 125, 2276
Brainerd, T. G., Blandford, R. D., & Smail, I. 1996, ApJ, 466, 623+
Broadhurst, T. J., Taylor, A. N., & Peacock, J. A. 1995, ApJ, 438, 49
Brown, M. L., Taylor, A. N., Hambly, N. C., & Dye, S. 2002, MNRAS, 333, 501
Connolly, A. J. & Szalay, A. S. 1999, AJ, 117, 2052
Connolly, A. J., Szalay, A. S., Bershady, M. A., Kinney, A. L., & Calzetti, D. 1995, AJ, 110, 1071
Crittenden, R. G., Natarajan, P., Pen, U., & Theuns, T. 2001, ApJ, 559, 552
Croft, R. A. C. & Metzler, C. A. 2000, ApJ, 545, 561
Csabai, I., Connolly, A. J., Szalay, A. S., & Budavári, T. 2000, AJ, 119, 69
Csabai, I. et al. 2003, AJ, 125, 580
Davis, M. & Geller, M. J. 1976, ApJ, 208, 13
Davis, M. & Peebles, P. J. E. 1983, ApJ, 267, 465
dell'Antonio, I. P. & Tyson, J. A. 1996, ApJ, 473, L17+
Eisenstein, D. J. et al. 2001, AJ, 122, 2267
Fischer, P. et al. 2000, AJ, 120, 1198
Frieman, J. A. & Gaztañaga, E. 1999, ApJ, 521, L83
Fukugita, M. et al. 1996, AJ, 111, 1748
Gòrski, K. M. et al. 1998, in press (astro-ph/9812350)
Griffiths, R. E., Casertano, S., Im, M., & Ratnatunga, K. U. 1996, MNRAS, 282, 1159
Gunn, J. E. et al. 1998, AJ, 116, 3040
Guzik, J. & Seljak, U. 2001, MNRAS, 321, 439
—. 2002, MNRAS, 335, 311
Heavens, A., Refregier, A., & Heymans, C. 2000, MNRAS, 319, 649
Heymans, C. et al. 2003, in press (astro-ph/0310174)
Hirata, C. M. & Seljak, U. 2002, in press (astro-ph/0301054)
Hoekstra, H., Franx, M., Kuijken, K., Carlberg, R. G., & Yee, H. K. C. 2003a, MNRAS, 340, 609
Hoekstra, H., van Waerbeke, L., Gladders, M. D., Mellier, Y., & Yee, H. K. C. 2002a, ApJ, 577, 604
Hoekstra, H., Yee, H. K. C., & Gladders, M. D. 2001, ApJ, 558, L11
—. 2002b, ApJ, 577, 595
Hoekstra, H. et al. 2003b, Submitted to ApJ, in press (astro-ph/0306515)
Hogg, D. W., Finkbeiner, D. P., Schlegel, D. J., & Gunn, J. E. 2001, AJ, 122, 2129
Hotelling, H. 1933, J. Educ. Psychol., 24, 417
Hudson, M. J., Gwyn, S. D. J., Dahle, H., & Kaiser, N. 1998, ApJ, 503, 531

Jarvis, M. et al. 2003, AJ, 125, 1014
Kaiser, N. 1984, ApJ, 284, L9
—. 1995, ApJ, 439, L1
Kaiser, N., Gahlman, G., & Woods, D. 1994, in Clusters of Galaxies, ed. F. Durret (Gif-sur-Yvette: Editions Frontieres)
Kaiser, N., Squires, G., & Broadhurst, T. 1995, ApJ, 449, 460+
Karhunen, K. 1947, Ann. Acad. Sci. Fennicae, 137
Koester, B. et al. 2003, in preparation
Loève, M. 1948, in Processes Stochastique et Mouvement Brownien, ed. P. Levy (Hermann, Paris)
Luppino, G. A. & Kaiser, N. 1997, ApJ, 475, 20
Lupton, R. H. et al. 2001, in ASP Conf. Ser. 238: Astronomical Data Analysis Software and Systems X, 269–+ (astro–ph/0101420)
McKay, T. A. et al. 2002, in press, (astro-ph/0108013)
Miralda-Escude, J. 1991, ApJ, 370, 1
Norberg, P. et al. 2001, MNRAS, 328, 64
—. 2002, MNRAS, 332, 827
Peacock, J. A. et al. 2001, Nature, 410, 169
Pen, U. 1998, ApJ, 504, 601+
Pen, U., Lee, J., & Seljak, U. 2000, ApJ, 543, L107
Percival, W. J. et al. 2001, MNRAS, 327, 1297
Pier, J. R. et al. 2003, AJ, 125, 1559
Richards, G. T. et al. 2002, AJ, 123, 2945
Saunders, W., Rowan-Robinson, M., & Lawrence, A. 1992, MNRAS, 258, 134
Schneider, P. & Seitz, C. 1995, A&A, 294, 411
Scranton, R. et al. 2002, ApJ, 579, 48
—. 2003, Phys. Rev. Lett., submitted, in press (astro-ph/0307335)
Seljak, U. et al. 2004, in preparation
Smith, D. R., Bernstein, G. M., Fischer, P., & Jarvis, M. 2001, ApJ, 551, 643
Smith, J. A. et al. 2002, AJ, 123, 2121
Spergel, D. N. et al. 2003, ApJ accepted, in press (astro-ph/0302209)
Stoughton, C. et al. 2002, AJ, 123, 485
Strauss, M. A. et al. 2002, AJ, 124, 1810
Szapudi, I. et al. 2002, ApJ, 570, 75
Tegmark, M. et al. 2004, Submitted to ApJ
Verde, L. et al. 2002, MNRAS, 335, 432
Wilson, G., Kaiser, N., Luppino, G. A., & Cowie, L. L. 2001, ApJ, 555, 572
York, D. G. et al. 2000, AJ, 120, 1579
Zehavi, I. et al. 2002, ApJ, 571, 172
—. 2003, Submitted to AJ, in press (astro-ph/0301280)
—. 2004, in preparation

Sheldon et al.

TABLE 1. MODEL FITS FOR DIFFERENT LENS SAMPLES

Sample	Selection Criteria	Mean Abs. Mag.	Mean $g-r$	N_{Lenses}	r_0	γ	χ^2/ν
All	-	-20.767 (1.455 ± 0.004)	0.629	127001	5.4 ± 0.7	1.79 ± 0.06	17.1/15
Red	$g-r > 0.7$	-21.061 (1.908 ± 0.006)	0.753	60099	6.9 ± 0.8	1.81 ± 0.05	12.3/15
Blue	$g-r < 0.7$	-20.477 (1.114 ± 0.004)	0.536	65134	4.0 ± 1.0	1.76 ± 0.15	5.97/6
Early	ECLASS < -0.06	-21.036 (1.864 ± 0.006)	0.737	62340	7.3 ± 0.8	1.77 ± 0.05	16.9/15
Late	ECLASS > -0.06	-20.474 (1.111 ± 0.004)	0.539	64378	3.3 ± 1.0	1.89 ± 0.17	7.18/6
Vlim	$-23.0 < M_r < -21.5$	-21.854 (3.961 ± 0.012)	0.718	10277	5.1 ± 0.8	2.01 ± 0.07	24.6/15
	$0.1 < z < 0.174$						

NOTE. — Absolute magnitudes are r-band Petrosian $M - 5\log_{10} h$. Values in parentheses are luminosity in units of $10^{10}h^{-2}L_\odot$. The means are calculated using the same weights as the lensing measurement. The value of $M_*(L_*)$ for the r-band is -20.83 (1.54). The r_0 and γ are best fit parameters for $\xi_{gm} = (r/r_0)^{-\gamma}$; r_0 is measured in h^{-1} Mpc. A value of $\Omega_m = 0.27$ was assumed. For the "late" and "blue" samples, the data were rebinned from 17 to 8 radial bins.

TABLE 2. LUMINOSITY BINS FOR ALL GALAXIES

Bandpass	Abs. Mag. Range	Mean Abs. Mag.	Mean $g-r$	N_{Lenses}	r_0	γ	χ^2/ν
u	$-19.6 < M_u < -15.0$	-18.515 (0.908 ± 0.002)	0.628	106585	5.5 ± 0.8	1.75 ± 0.06	13.5/15
-	$-20.0 < M_u < -19.6$	-19.763 (2.864 ± 0.003)	0.639	12539	4.4 ± 0.8	2.04 ± 0.09	19.2/15
-	$-22.0 < M_u < -20.0$	-20.318 (4.779 ± 0.020)	0.654	6270	6.9 ± 1.0	1.97 ± 0.07	26.3/15
g	$-21.0 < M_g < -16.5$	-19.891 (0.956 ± 0.002)	0.623	106646	5.4 ± 0.9	1.75 ± 0.07	15.1/15
-	$-21.4 < M_g < -21.0$	-21.188 (3.156 ± 0.004)	0.699	12546	5.0 ± 0.8	2.02 ± 0.08	12.7/15
-	$-23.5 < M_g < -21.4$	-21.718 (5.145 ± 0.025)	0.734	6275	7.0 ± 0.8	2.03 ± 0.06	24.6/15
r	$-21.7 < M_r < -17.0$	-20.544 (1.184 ± 0.003)	0.621	106643	5.4 ± 0.8	1.74 ± 0.07	15.9/15
-	$-22.2 < M_r < -21.7$	-21.902 (4.137 ± 0.005)	0.726	12543	5.2 ± 0.8	2.03 ± 0.07	13.5/15
-	$-24.0 < M_r < -22.2$	-22.463 (6.937 ± 0.026)	0.767	6274	7.5 ± 0.8	2.01 ± 0.05	30.9/15
i	$-22.0 < M_i < -17.0$	-20.870 (1.446 ± 0.003)	0.620	106625	5.3 ± 0.9	1.74 ± 0.07	17.6/15
-	$-22.5 < M_i < -22.0$	-22.232 (5.067 ± 0.006)	0.734	12544	5.1 ± 0.7	2.04 ± 0.07	19.3/15
-	$-24.0 < M_i < -22.5$	-22.776 (8.368 ± 0.030)	0.772	6271	6.9 ± 0.8	2.06 ± 0.06	24.7/15
z	$-22.2 < M_z < -17.0$	-21.069 (1.721 ± 0.004)	0.619	105975	5.3 ± 0.9	1.73 ± 0.07	16.8/15
-	$-22.6 < M_z < -22.2$	-22.350 (5.599 ± 0.007)	0.725	12466	5.5 ± 0.8	1.97 ± 0.07	20.3/15
-	$-24.0 < M_z < -22.6$	-22.881 (9.132 ± 0.032)	0.753	6236	6.6 ± 0.8	2.05 ± 0.06	22.1/15

NOTE. — Galaxies were split into three bins of absolute magnitude in each of the five SDSS bandpasses, as listed in column two. See table 1 for explanations of the other columns. The value of $M_*(L_*)$ is -18.34(0.77), -20.04(1.10), -20.83(1.54), -21.26(2.07), -21.55(2.68) for u, g, r, i, z respectively.

TABLE 3. LUMINOSITY BINS FOR RED GALAXIES

Bandpass	Abs. Mag. Range	Mean Abs. Mag.	Mean $g-r$	N_{Lenses}	r_0	γ	χ^2/ν
u	$-19.6 < M_u < -15.0$	-18.521 (0.913 ± 0.003)	0.752	51074	6.9 ± 0.9	1.77 ± 0.06	10.0/15
-	$-20.1 < M_u < -19.6$	-19.791 (2.939 ± 0.005)	0.769	6008	5.6 ± 0.8	2.09 ± 0.07	21.6/15
-	$-22.0 < M_u < -20.1$	-20.373 (5.026 ± 0.027)	0.789	3006	9.6 ± 1.1	1.96 ± 0.06	35.2/15
g	$-21.2 < M_g < -16.5$	-20.112 (1.171 ± 0.003)	0.752	51084	7.0 ± 1.0	1.75 ± 0.06	9.46/15
-	$-21.6 < M_g < -21.2$	-21.364 (3.712 ± 0.006)	0.773	6008	6.4 ± 0.7	2.04 ± 0.06	20.8/15
-	$-23.5 < M_g < -21.6$	-21.841 (5.762 ± 0.025)	0.788	3006	8.9 ± 0.9	2.03 ± 0.05	40.2/15
r	$-21.9 < M_r < -17.0$	-20.867 (1.596 ± 0.005)	0.751	51080	7.0 ± 1.0	1.75 ± 0.06	9.56/15
-	$-22.4 < M_r < -21.9$	-22.140 (5.152 ± 0.009)	0.775	6008	6.6 ± 0.8	2.03 ± 0.06	19.0/15
-	$-24.0 < M_r < -22.4$	-22.635 (8.127 ± 0.037)	0.793	3004	9.0 ± 0.9	2.03 ± 0.05	34.3/15
i	$-22.3 < M_i < -17.0$	-21.240 (2.033 ± 0.006)	0.751	51078	6.9 ± 1.0	1.76 ± 0.06	10.1/15
-	$-22.7 < M_i < -22.3$	-22.478 (6.354 ± 0.011)	0.776	6007	7.1 ± 0.9	1.98 ± 0.06	20.9/15
-	$-24.0 < M_i < -22.7$	-22.946 (9.778 ± 0.043)	0.790	3005	8.4 ± 0.8	2.06 ± 0.05	35.0/15
z	$-22.4 < M_z < -17.0$	-21.412 (2.360 ± 0.007)	0.751	50697	7.0 ± 1.0	1.75 ± 0.06	10.1/15
-	$-22.8 < M_z < -22.4$	-22.563 (6.810 ± 0.011)	0.772	5962	5.4 ± 0.9	2.06 ± 0.08	8.99/15
-	$-24.0 < M_z < -22.8$	-23.045 (10.61 ± 0.048)	0.782	2983	7.2 ± 0.9	2.09 ± 0.06	26.0/15

NOTE. — Same as table 2 but for red galaxies, defined as galaxies with $g-r > 0.7$.